

Dynamics of droplets and bubbles coated with magnetic particles

Zhao, Xue

2009

Zhao, X. (2009). Dynamics of droplets and bubbles coated with magnetic particles. Doctoral thesis, Nanyang Technological University, Singapore.

<https://hdl.handle.net/10356/19013>

<https://doi.org/10.32657/10356/19013>



**NANYANG
TECHNOLOGICAL
UNIVERSITY**

DYNAMICS OF DROPLETS AND BUBBLES
COATED WITH MAGNETIC PARTICLES

**DYNAMICS OF DROPLETS AND BUBBLES COATED
WITH MAGNETIC PARTICLES**

ZHAO XUE

ZHAO XUE

SCHOOL OF PHYSICAL AND MATHEMATICAL SCIENCES

2009

2009

**DYNAMICS OF DROPLETS AND BUBBLES COATED
WITH MAGNETIC PARTICLES**

ZHAO XUE

School of Physical and Mathematical Sciences

A thesis submitted to the Nanyang Technological University

in fulfillment of the requirement for the degree of
Doctor of Philosophy

2009

ACKNOWLEDGMENTS

I am greatly indebted to my supervisors Asst. Prof. Claus-Dieter Ohl and Prof. Lars Egil Helseth for the support they have extended to me throughout my work towards this thesis, and for their informed guidance and advice.

I also extend my sincere gratitude to Prof. Shen Zexiang and Prof. Huan Cheng Hon who offered me encouragement when I felt frustrated and helpless.

I would also like to thank Dr Pedro Antonio Quinto Su for his warm-hearted and patient help with the bubble oscillation experiments and discussions.

Many thanks also go to Asst. Prof. Chew Lock Yue, Asst. Prof. Wu Tao, Asst. Prof. Yu Ting, Asst. Prof. Rainer Dumke, all my colleagues, Mr. Miao Yuanhua, Mr. Geng Dalong, Mr. Tao Junguang, Dr. Ni Zhenhua, Mr. You Yumeng, Mr. Johnson Kasim, Ms. Ma Yun, Mr. Zheng Zhe...from School of Physical and Mathematical Sciences of NTU, for their kindly help.

This thesis is dedicated to my parents, Zhao Chunhai and Wang Junrong, my husband Lu Weihan, my friend Wang Yingying, who have always stood by my side, always given me the strength and encouragement, and have never left me in doubt of their love for me.

Table of contents

ACKNOWLEDGMENTS	i
Table of contents	ii
Summary	v
Publications	vii
Chapter 1	1
Introduction	1
1.1 Wetting properties of particles	1
1.2 Emulsions stabilized by particles	3
1.3 Colloidosomes	7
1.4 Magnetic properties of magnetic nanoparticles	9
1.5 Transport of liquid droplets	13
1.6 Bubbles covered by particles	16
1.7 Applications of bubbles driven by a sound field	20
1.8 A guide through the chapters	21
Chapter 2	23
Magnetophoresis of microspheres covered by magnetic nanoparticles	23
2.1 Introduction	23
2.2 Experimental methods	24
2.2.1 Materials	24
2.2.2 Preparation of magnetic nanoparticles	25
2.2.3 Preparation of magnetic microspheres	26
2.3 Results	28
2.4 Discussion	30
2.5 Conclusion	36
Chapter 3	38
Transport of free-floating droplets using electromagnetic coils	38
3.1 Introduction	38
3.2 Experimental methods	39
3.3 Results and discussion	43
3.4 Conclusion	47
Chapter 4	48
Dynamics of magnetic bubbles in acoustic and magnetic fields	48
4.1 Introduction	48
4.2 A microscopic look at the magnetic bubbles	49
4.3 Magnetic susceptibility of magnetic bubbles	51
4.4 The oscillation of magnetic bubbles	55
4.5 Conclusion	58
Chapter 5	59
Translation of an oscillating and rising magnetic bubble	59
5.1 Introduction	59
5.2 Experimental methods	60
5.3 Results and discussion	62

5.4 Conclusion	68
Chapter 6	69
Conclusions and Future Work	69
6.1 Conclusions.....	69
6.2 Future work.....	70
References.....	72

Nomenclature

a	Acceleration
b_1	Half major axis of an ellipse
b_2	Half minor axis of an ellipse
B	Magnetic fields
C_d	Drag coefficient
d	Diameter
ΔE_1	The energy required to bring the particle from the interface back to the oil phase
ΔE_2	The energy required to bring the particle from the interface back to the water phase
f	Frequency
F	Force
g	Acceleration of gravity
H	Magnetic field strength
I	Electric current
k_B	Boltzmann constant
L	Distance between tips and the water surface
m	Magnetic moment
M	Magnetization
n	Number of nanoparticles
r	Radius
R	Ratio
Re	Reynolds number

s	Distance
t	Time
T	Room temperature
U	Magnetic potential energy
v	Velocity
V	Volume
γ	Surface tension
γ_{ow}	Surface tension of the oil-water interface
γ_{so}	Surface tension of the solid-oil interface
γ_{sw}	Surface tension of the solid-water interface
η	Dynamic viscosity of the liquid
θ	Contact angle
μ_0	Vacuum magnetic permeability
ν	Kinematic viscosity of the liquid
ρ	Density of the liquid
φ	Phase constant
χ	Volume magnetic susceptibility
χ_b	Magnetic susceptibility of the bubble
χ_m	Volume magnetic susceptibility of the nanoparticles
χ_{sphere}	Magnetic susceptibility of the microsphere

Summary

Based on the interfacial self-assembly of magnetic nanometer and micrometer sized particles, we demonstrate the formation of microspheres covered by magnetic nanoparticles, millimeter-sized oil droplets stabilized by a layer of closely-packed microparticles, and a new type of bubble with a permanent magnetization.

The motion of individual magnetic microspheres in a defined magnetic field gradient is investigated and the susceptibilities of individual magnetic microspheres are estimated. Our measurement shows that the magnetic moment of the microspheres scales with their diameters. This is reasonable since the magnetic nanoparticles are attached to the surface of these microspheres, which means the larger the surface area, the more possibilities for these magnetic nanoparticles to attach to the surface.

We describe a liquid-liquid microfluidic system for transporting millimeter-sized oil droplets coated with paramagnetic microparticles, which float freely at the air-water interface and are driven by a magnetic field applied with a pair of electromagnetic coils above the surface of the water phase. Material can be dispersed inside oil droplets and the influence on it, for example, particles may absorb to or react with delivered material, can be minimized since magnetic colloids, the surface of which can be modified with certain functional groups, are located on the surface of droplets.

The experiments conducted to study bubble oscillations in weak acoustic fields show that magnetic bubbles are compressible in moderate acoustic fields and can induce a microstreaming flow with a toroidal vortex at the bubble's upper pole.

Similar microstreaming flows have been used to transport and rupture cells at small scales. Thus we envision applications in manipulation of biological materials and in microfluidic devices using acoustic and magnetic forces.

We investigate the impact of a magnetic bubble's volume oscillation on its mean rise velocity. The experiments clearly show that the volume oscillating magnetic bubble after the acoustic field is switched on has 3% higher mean rise velocity than the non-oscillating magnetic bubble. With the help of a force balance model we find that the increase of mean rise velocity is due to an added-mass effect.

Publications

Journal publications

1. **Zhao X.**, Helseth L.E. *Magnetophoresis of microspheres covered by magnetic nanoparticles* **Journal of Applied Physics** 102, 054905 (2007). It has been selected for the September 24, 2007 issue of **Virtual Journal of Nanoscale Science & Technology** which covers a focused area of frontier research.
2. **Zhao X.**, Quinto-Su P. A., Ohl C. D., *Dynamics of magnetic bubbles in acoustic and magnetic fields* **Physical Review Letters** 102, 024501 (2009). It is covered by **Physics Today's Physics Update** 12th January 2009.

Conference talks and poster presentations

I gave a presentation entitled “Magnetic Bubbles” at the Division of Fluid Dynamics Meeting of the American Physical Society (APS/DFD) in November 2008 in San Antonio, TX.

I presented at the APS the poster “Cavitation within a droplet” which won the Gallery of Fluid Motion Award at the APS/DFD 2008 meeting.

Chapter 1

Introduction

1.1 Wetting properties of particles

It is well established that fine solid particles can spontaneously adsorb onto the interface (water-air or water-oil), when the interfacial tensions of the solid-oil or air (SO), solid-water (SW) and oil or air-water (OW) satisfy the condition $|\gamma_{SO} - \gamma_{SW}| < \gamma_{OW}$ [1], where γ is the respective coefficient of surface tension. Let's consider a spherical particle which is initially fully submerged in the water phase and subsequently adsorbs onto a water-oil interface as shown in Figure 1.1. Ignoring the line tension acting at the three-phase contact line, adsorption of the particle at the interface results in an area of the solid-water interface being lost but an equal area of the solid-oil interface being gained. Furthermore, an area of the planar oil-water interface is also lost due to the presence of the particle [2]. Its equilibrium angle at the three-phase line of contact is characterized by contact angle θ which is determined via Young's equation

$$\cos \theta = (\gamma_{SO} - \gamma_{SW}) / \gamma_{OW} \quad (1.1)$$

in the absence of line tension, where γ_{SO} , γ_{SW} and γ_{OW} are the interfacial tensions of the solid-oil (SO), solid-water (SW), and oil-water (OW) interfaces respectively.

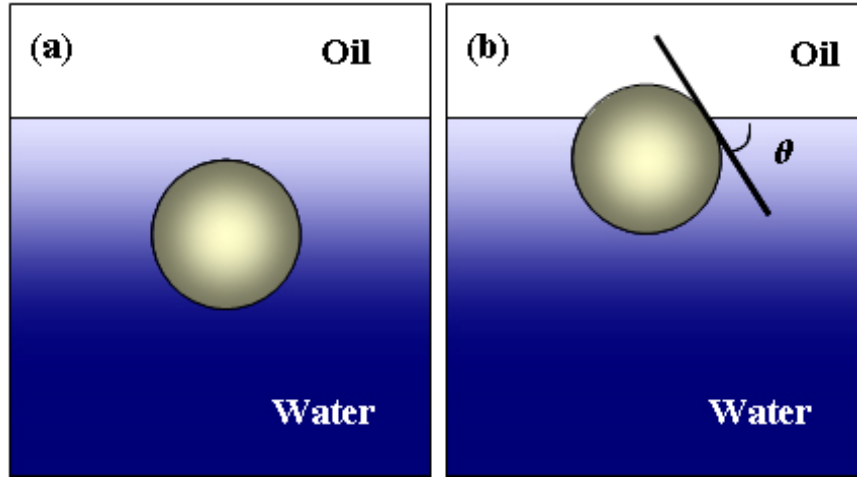


Figure 1.1: (a) A small spherical solid particle is initially immersed in water phase. (b) It is subsequently adsorbed to the water-oil interface with contact angle θ (measured through the aqueous phase).

The energy of adsorption of a particle to the water-oil interface depends on the contact angle as well as the surface tension of the interface. Assuming the particle is small enough (typically less than a few micrometers in radius) so that the effect of gravity is negligible, the energy which is required to bring the particle from the interface back to the oil phase [2] is

$$\Delta E_1 = \pi r^2 \gamma_{ow} (1 + \cos \theta)^2 \quad (1.2)$$

or

$$\Delta E_2 = \pi r^2 \gamma_{ow} (1 - \cos \theta)^2 \quad (1.3)$$

back into the water phase, where r is the radius of the particle, θ is the contact angle of the particle and γ_{ow} is the oil-water surface tension. Inspection of Eq. (1.2) and (1.3) for given $r = 1.4 \times 10^{-8} m$ (characteristic of magnetic nanoparticles, later) and $\gamma_{ow} = 52.5 \pm 0.4 mNm^{-1}$ (for hexadecane-water interface) shows that the particle is

most strongly held at the interface for $\theta = 90^\circ$ with $\Delta E_1 = \Delta E_2 = 7.9 \times 10^3 k_B T$ (k_B is Boltzmann constant and $T = 296$ K is the room temperature.). This high energy required to resuspend the particle as compared with the thermal energy $k_B T$, allows characterizing the particle in this size as irreversibly adsorbed onto the interface. ΔE_1 decreases to zero when θ increases from 90° to 180° ; ΔE_2 decreases to zero when θ decreases from 90° to 0° . For $\theta < 90^\circ$ the particle is more easily brought back to water than to oil ($\Delta E_1 > \Delta E_2$), and for $\theta > 90^\circ$ the reverse is true ($\Delta E_1 < \Delta E_2$).

1.2 Emulsions stabilized by particles

Nanometer to micrometer-sized solid particles with suitable wettabilities are able to stabilize emulsions effectively by adsorbing onto the oil-water interface. Effectiveness of solid particles in stabilizing emulsions relies on particle properties, such as size, wettability, shape, particle concentration and interparticle interactions. Emulsion stabilization is achieved when the particles diffuse to the water-oil interface and stay there in a stable mechanical equilibrium. Rigid structures are usually developed by the particles at the interfacial region, thus preventing coalescence when droplets come near to each other. Solid-stabilized emulsions are encountered in products in food, medicine, paint and oil industries, where emulsion stability against coalescence is important. As a result, It is essential to understand the mechanisms controlling the stability of these emulsions.

The role of finely divided solid particles has been recognized as the stabilizer in emulsions since the beginning of the last century. Pickering [3] observed that colloidal particles which were wetted more by water than by oil could stabilize

oil-in-water emulsions. These are mentioned as either solid-stabilized emulsions or Pickering emulsions. Since then, many researchers have investigated the stability of Pickering emulsions. The early studies by Finkle et al. [4] recognized the relationship between the wettability of the particles and the type of emulsion stabilized by the particles. They observed that particles wetted more by water stabilized oil-in-water emulsions, while the particles wetted more by oil stabilized water-in-oil emulsions. These ideas were further supported by the experiments of Schulman and Leja [5] with BaSO₄ powders, whose contact angles were controlled by adsorption of surfactants. They demonstrated if the contact angle of the solid particles at the solid-oil-water interfaces was slightly less than 90⁰, the particles stabilized oil-in-water emulsions. If the contact angle was somewhat greater than 90°, the particles stabilized water-in-oil emulsions. If the particles were completely wetted either by the water or by the oil, no stable emulsions were formed. Similar results were reported by Binks and Lumsdon [6]. They studied the effect of the wettability of nanometer-sized silica particles on the stability and type of emulsions of water and toluene. They observed that emulsions stabilized by particles of intermediate hydrophobicity were stable to coalescence indefinitely while emulsions stabilized by either very hydrophobic or hydrophilic particles were unstable to coalescence. Binks and Lumsdon [7] also studied the stability of emulsions of oil and water stabilized only by spherical, monodisperse polystyrene latex particles in different diameters. With the freeze fracture scanning electron microscopy measurements on these emulsions, they confirmed that the emulsifiers of the water-in-cyclohexane emulsions were solid particles adsorbed onto the water-cyclohexane interface. On the emulsion droplet surface there were areas where monodisperse particles were close-packed, but there were also areas where small gaps came into sight between particle arrays.

Ashby and Binks [8] studied the stability and type of solid-stabilized emulsions using disc-like Laponite clay particles as stabilizers. They observed that stable toluene-in-water emulsions were formed only if the particles were flocculated by adding salt (NaCl) and at intermediate concentrations of clay particles. Neither gel nor discrete particle dispersions were able to form stable emulsions against coalescence. Abend et al. [9] studied stabilization of paraffin-water emulsions by mixtures of oppositely charged colloidal particles: a layered double hydroxide with positive charges and the clay mineral montmorillonite with negative charges. They observed that the stability of the emulsion was not affected by the mixing ratio of two types of colloidal particles when the overall solid content was larger than 0.5%. Binks et al. [10] studied the stabilization of emulsions by a mixture of silica nanoparticles with opposite signs of charge in connection with their behavior in water before emulsification. They observed neither positively nor negatively charged silica particles alone could stabilize emulsions, however certain mixtures of two types of particles which resulted in heteroaggregation were able to create stable oil-in-water emulsions against coalescence.

A theory concerning the adsorption energy of solid particles onto a liquid-liquid interface was developed by Levine et al. [2]. They concluded that an isolated particle with a proper contact angle at the surface of an oil-in-water emulsion droplet was trapped in a very deep energy well. Interfacial particles were capable of forming a close-packed, coherent film which acted as a barrier, hindering the necessary close contact for the droplets to coalesce. Denkov et al. [11] investigated films composed of a particle monolayer and the stability of the liquid menisci between the particles theoretically. They proposed the capillary pressure caused by the deformed liquid interface around the colloidal particles could be the factor avoiding the thinning of the

liquid film between the droplets. Tsugita et al. [12] studied stable O/W emulsions by using combinations of Na-montmorillonite and polar organic compounds such as ethyleneglycol monostearate. They observed that interfacial film consisting of the complex formed by Na-montmorillonite and particular polar organic compounds prevented the coalescence of oil droplets. The network structure formed by montmorillonite in the water which fixed the oil droplets and prevented the drainage of the aqueous phase also contributed to the stabilization of emulsions. Similar results have been reported by Tambe and Sharma [13]. They attributed the stability of solids-stabilized emulsions to the steric hindrance provided by colloidal particles and the rheological properties of the interface which controlled the drainage of the thin liquid films between the droplets.

Although the large number of studies on the stability of Pickering emulsions have been carried out, the mechanism of emulsion stabilization by colloidal particles is still inadequately understood. However some general trends and conditions have been well recognized [13]: (i) The particles must have the ability to diffuse to the water-oil interface and remain there in a stable equilibrium position before any stable solid-stabilized emulsions can be formed. (ii) The interfacial film formed by colloidal particles which possesses certain interfacial rheological properties is essential to stabilize emulsions. (iii) Particles wetted more by water phase tend to stabilize oil-in-water emulsions, while particles wetted more by oil phase tend to stabilize water-in-oil emulsions. (iv) Some degree of particles interactions is important to the stability of these emulsions.

1.3 Colloidosomes

The mechanism that finely divided particles can spontaneously adsorb onto oil-water interface has also been used to fabricate colloidosomes by the self-assembly of particles onto the interface of emulsion droplets. Colloidosomes are capsules, whose surfaces are formed by a close-packed layer of colloidal particles linked together. The phase inside the shells of colloidosomes is the same as the phase outside the shells of colloidosomes. While emulsions are oil droplets in the water phase or water droplets in the oil phase with particles at the oil-water interface.

Dinsmore et al. [1] presented a flexible approach to prepare colloidosomes with sizes in the range between micrometers and millimeters and with easily controllable elasticity and permeability. Their approach used controlled self-assembly of colloidal particles in three steps shown in Figure 1.2. First, aqueous solution containing the material to be encapsulated was added to oil containing colloidal particles. Aqueous droplets were formed with the surfaces densely covered by colloidal particles by gentle continuous shearing for several seconds. Second, the particles were locked together to form an elastic shell by sintering the particles, by addition of polycations, or by van der Waals forces. Lightly sintering the particles could achieve precisely controlled permeability which were determined by the interstices between the particles. Upon heating, the particles started to coalesce. An increase in the sintering time resulted in smaller pores as well as higher rupture stress of the colloidosomes. Third, the capsules were transferred into a liquid which was the same as the dispersed phase by centrifugation. This step allowed the pores of the capsules to control its permeability by removing the interface between the external and internal fluids. The choice of a wide variety of fluids and colloidal particles offered extra flexibility.

Furthermore, a number of potential mechanisms for release, such as sustained release through the controlled pores and rupture of the elastic shells through shear stress, made them promising as encapsulants.

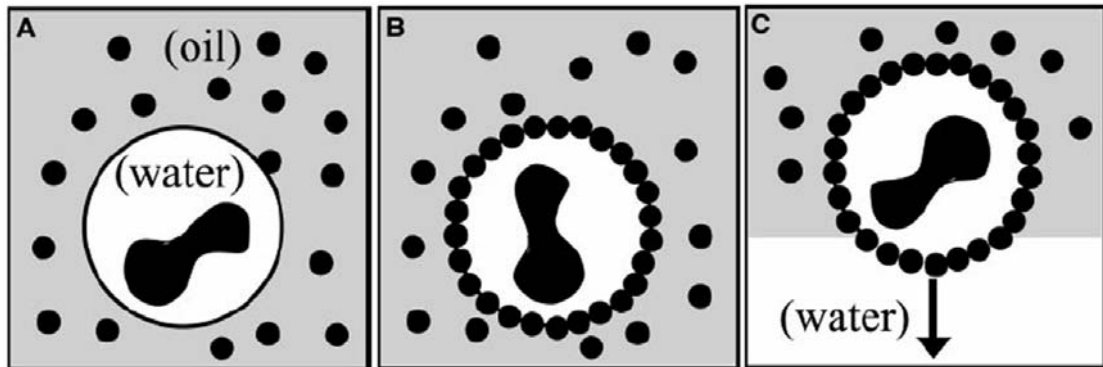


Figure 1.2: Schematics of the self-assembly process for colloidosomes. (A) Aqueous solution was added to oil which contained colloidal particles. Aqueous droplets were created by continuous shearing. (B) Particles adsorbed onto the surface of the droplet and were subsequently locked together by sintering the particles, by addition of polycations, or by van der Waals forces. (C) The capsule was transferred by centrifugation into the water phase. Taken from ref. [1].

Samanta et al. [14] reported the fabrication of stable magnetite colloidosomes by crosslinking magnetic nanoparticles at the water-oil interface using a Huisgen click reaction under ambient conditions. Duan et al. [15] also made magnetic colloidosomes with shells consisting of monolayer of closed-packed magnetite nanoparticles. The nanoscale permeability of the shell could be controlled by the size of the nanoparticles used. In addition, these magnetic colloidosomes allowed

manipulation by applying an external magnetic field which was a promising feature in targeted delivery.

1.4 Magnetic properties of magnetic nanoparticles

Magnetic particles have been used to stabilize emulsions and fabricate colloidosomes since they can spontaneously adsorb onto the oil-water interface. Additionally, They can be manipulated by an external magnetic field gradient and their surface can be modified with biocompatible molecules. These special properties open up many applications. Magnetic particles are used to label specific biological entities in magnetic separation [16], to deliver drugs to target specific sites within the body [16], as magnetic labels for detection of target molecules in biosensors [17], or for microfluidic applications in lab-on-a-chip systems [18]. Consequently, careful magnetic characterization of these magnetic particles is required for the purpose of applications.

Gill et al. [19] proposed a method for measuring the magnetic susceptibilities of small particles of diameters ranging from 1 to 100 μm , such as red blood cells and polystyrene latexes. Their method measured the magnetic susceptibility by determining the motion of particles with the magnetic susceptibility different from that of the surrounding liquid in a magnetic field gradient. A similar approach was also used by Hafeli et al. [20] to measure the magnetophoretic mobility of individual magnetic microspheres of diameters of 1 to 3.6 μm in a defined magnetic field. They concluded that the magnetophoretic mobility of magnetic microspheres relied not only on type, amount and distribution of encapsulated magnetic material, but also on

porosity, solvent system and other factors. However, for particles smaller than 1 μm , it is very difficult to measure their magnetic susceptibilities accurately due to Brownian motion. Ommering and Nieuwenhuis [21] broke this 1 μm barrier by exploiting the Brownian motion. They calculated the magnetic susceptibilities of nanoparticles of diameters of 150-450 nm by analyzing the confined Brownian motion of individual nanoparticles confined in a magnetic potential well on a chip. They found nanoparticles of the same size could have susceptibilities which differed more than a factor of 2.

To understand magnetic properties of magnetic nanoparticles, we start from the relevant basic concepts of magnetism. When a magnetic material is placed in an external magnetic field of strength \vec{H} , the magnetic induction is

$$\vec{B} = \mu_0(\vec{H} + \vec{M}), \quad (1.4)$$

where μ_0 is the vacuum magnetic permeability, and \vec{M} is magnetization defined as the quantity of magnetic moment per unit volume

$$\vec{M} = \vec{m}/V, \quad (1.5)$$

where \vec{m} is the magnetic moment on a volume V of the material. Magnetic materials may be classified in terms of volume magnetic susceptibility χ , which is the degree of magnetization of a material in response to an applied magnetic field. It is defined by the relationship

$$\vec{M} = \chi \vec{H}. \quad (1.6)$$

In SI units both \vec{M} and \vec{H} are measured in amperes per meter, therefore χ is dimensionless. Most materials have weak magnetism in the presence of an applied field; they are referred to either as paramagnets or diamagnets. The magnetization of paramagnets responds in the same direction as the external field with χ in the range 10^{-6} - 10^{-1} ; while the magnetization of diamagnets responds in the opposite direction

with χ ranging from -10^{-6} to -10^{-3} . However, some materials display ordered magnetic states and are magnetic in the absence and presence of an external field; these are classified as ferrimagnets, ferromagnets and antiferromagnets, where the prefix relates to the characteristic of the coupling interaction between the electrons in the material [16].

The susceptibility of materials can be characterized by magnetization curve where the magnetization \vec{M} is plotted versus the magnetic field strength \vec{H} . For both ferromagnetic and ferrimagnetic materials, one often sees hysteresis loops in $M-H$ curve shown in Figure 1.3. It is an irreversibility in the magnetization process due to

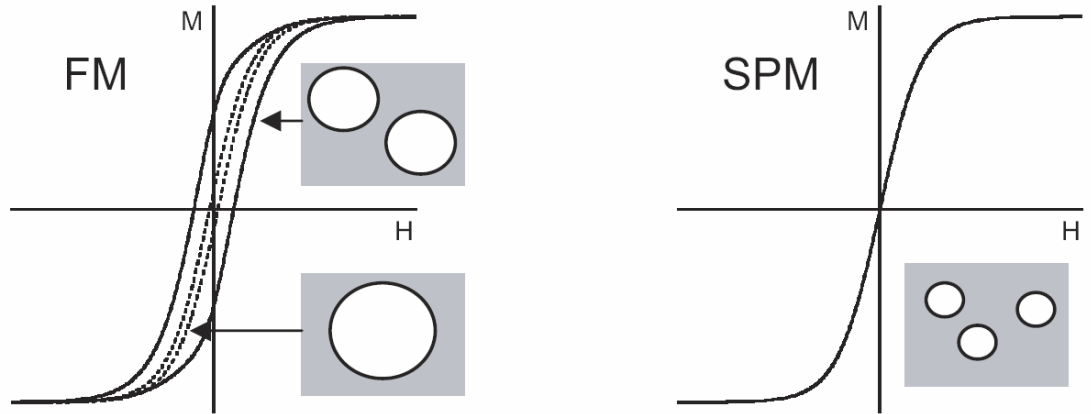


Figure 1.3: Magnetization curves were shown for ferromagnetic materials (FM), where the response could be multi-domain (a narrow hysteresis loop), single-domain (a broad hysteresis loop) and superparamagnetic (SPM), relying on the size of the particle. Taken from ref. [16].

the pinning of magnetic domain walls at grain boundaries and the magnetic anisotropy of the crystalline lattice. The shape of these loops partly depends on particle size:

large particles (a few micrometers in diameter or more) have a multi-domain ground state which results in a narrow hysteresis loop since moving the domain walls requires relatively little energy; while small particles have a single domain ground state which results in a wide hysteresis loop. When the sizes become even smaller (tens of nanometers in diameter or less), superparamagnetism occurs, where the curve does not show any hysteresis. Superparamagnetic particles do not possess permanent magnetic moments in the absence of an external field but can respond to an external magnetic field.

To understand how a magnetic field is used to manipulate magnetic objects in magnetic separation, drug delivery and magnetophoretic analysis, we need to discuss the magnetic force acting on the magnetic object. The magnetic potential energy U of the object in the magnetic field can be determined by taking the integral of the magnetization \vec{M} of the object and the magnetic field in the absence of the object \vec{B} over the volume of the object [21]

$$U = -\int \frac{1}{2} \vec{M} \cdot \vec{B} dV, \quad (1.7)$$

where \vec{B} is a vector defined as (B_x, B_y, B_z) and \vec{M} can be expressed as

$$\vec{M} = \chi \vec{H} = \chi \frac{\vec{B}}{\mu_0}. \quad (1.8)$$

We assume that the object is surrounded by a nonmagnetic liquid and that the magnetic field is constant over the volume of the object. In this way Eq. (1.7) can be written as

$$U = -\frac{\chi}{2\mu_0} V \vec{B}^2. \quad (1.9)$$

The magnetic force acting on the object, \vec{F} , is equal to $-\text{grad } U$ [22]. Therefore, the x, y, z component of the force can be written as

$$F_x = \frac{\chi V}{\mu_0} \bar{B} \frac{\partial \bar{B}}{\partial x}, \quad (1.10)$$

$$F_y = \frac{\chi V}{\mu_0} \bar{B} \frac{\partial \bar{B}}{\partial y}, \quad (1.11)$$

$$F_z = \frac{\chi V}{\mu_0} \bar{B} \frac{\partial \bar{B}}{\partial z}. \quad (1.12)$$

The strength of the magnetic force depends on the magnetic property of the object, magnetic field and field gradient. A uniform magnetic field does not cause translational action.

1.5 Transport of liquid droplets

Transport of liquid droplets is an important task in microfluidic systems [23]. Several methods for transporting droplets have been proposed including the use of thermalcapillary effect [24, 25], surface chemical gradients [26], light [27], electrostatic actuation [28], electrowetting [29], dielectrophoretic force [30], and magnetism [31-34].

Barton and Subramanian [24] reported transport of liquid droplets in a vertical temperature gradient. They observed droplets of pure ethyl salicylate which sank in diethylene glycol under isothermal conditions moved upward to regions of higher temperature. They found the observed motion was of thermocapillary origin which resulted from the interfacial tension gradients over the surface of the droplet due to the change in temperature. The thermocapillary contribution to the droplet velocities scaled with the droplet radius as well as the applied temperature gradient. Sammarco and Burns [25] reported transport of liquid droplets within microfabricated flow

channels by thermocapillary pumping. They heated one end of a single droplet to create a surface tension difference between the ends of the droplet which caused a capillary pressure difference and resulted in droplet motion. In contrast to thermocapillary transport, Chaudhury and Whitesides [26] reported transport of water droplets uphill by a spatial gradient in surface free energy of a solid substrate. By exposing the surface of a polished silicon wafer to the diffusing front of a vapor of decyltrichlorosilane, the substrate with the required gradient in surface free energy was obtained. They observed a droplet of water moved uphill with an average velocity of 1 to 2 millimeters per second uphill on the substrate tilted from the horizontal plane by 15° . They explained this motion resulted from the imbalance in the forces caused by surface tension acting on the solid–liquid contact line around the droplets. Ichimura et al. [27] reported the transport of liquid droplets by light when a substrate surface was modified with a photoisomerizable azobenzene monolayer. The transport of the droplet was guided by spatially controlled photoirradiation of photoresponsive substrate surface which generated photochemically a gradient in surface energy. The velocity and direction of the transport were controlled by changing the steepness and direction of the gradient in light intensity.

Washizu [28] developed a device for the electrostatic transport of water droplets on a solid surface by arrays of microelectrodes. The principle of the droplet actuation was the variable capacitance between the droplet and the electrode which was covered by a hydrophobic insulator layer. Pollack and Richard [29] reported rapid transport of droplets of polarizable and conductive liquid by direct electrical control of the surface tension using two groups of opposite planar electrodes made on glass. They observed the transport speed represented a almost 100-fold increase over previously reported electrical methods to transport droplets on solid surfaces. Velez et al. [30] described a

microfluidic system for transporting microlitre and nanolitre-sized droplets of water. The aqueous droplet floating on a perfluorinated oil was transported by an alternating electric field generated by arrays of electrodes under the oil. The water droplets moved more slowly by floating on the oil than in contact with electrodes on solid surface, but this system overcame the drawbacks of delivering materials such as biological cells, which might adhere to the solid surface.

Magnetic force is another option for the transport of liquid droplets with the advantage of the long range of the force and the little influence with non-magnetic substance. Ohashi et al.[31] reported transport of aqueous droplets by the use of both electrostatic and magnetic forces. Magnetic particles in diameters of 2-5 μm were included in a water droplet as force mediators. After the droplet was held at the bottom surface by electrostatic force, the magnetic particles carrying a small volume of droplet solution were separated from the droplet by a moving permanent magnet. Lehmann et al. [32] presented a system for the two-dimensional magnetic manipulation of aqueous droplets suspended in silicone oil as a platform for on-chip bioanalysis. Magnetic beads with diameters ranging from 250 nm to 6 μm were incorporated into the droplet to provide the means of the magnetic actuation. Their system used an array of planar microcoils to transport droplets instead of external moving magnets. The particles inside aqueous droplets were redistributed and dragged the droplet into the direction of the magnetic field gradient, by transferring their actuation force on the inner droplet-oil interface. Nguyen et al. [33] reported a system for magnetic transport of ferrofluid droplets. The magnetic field was also produced by an array of planar coils. The magnetic particles dispersed in the droplet had a diameter of the order of several nanometers. The dispersion of these particles did not redistribute under the magnetic field because their random movement was

stronger than the motion caused by the magnetic force. Hong et al. [34] reported direct transport of superparamagnetic droplets on superhydrophobic surfaces without any leaks by alternating magnetic fields. Superhydrophobic surfaces were capable of completely transporting water droplets without deposition of liquid on the solid surfaces. Furthermore, the strong adhesive force of the surface could hold the droplet in place without sliding. The magnitude and the direction of magnetic force controlled the transport of the superparamagnetic droplet. Their work offered an alternative way to overcome technological difficulties encountered through microfluidic systems: delivered materials might adhere to the solid walls and clog the channels because of the nature of the contact with the solid surfaces.

1.6 Bubbles covered by particles

Finely divided solid particles with proper hydrophobicity can adsorb onto the water-oil interface and act as effective stabilizing agents of emulsions. Surface active particles can also adsorb onto the water-air interface and stabilize bubbles and foams. Although many studies of stable bubbles covered with particles have been conducted, the stabilizing mechanism remains an open question.

Kam and Rossen [35] studied a two-dimensional theoretical model for bubbles coated by solid particles. Solid particles partly wetted by both gas and liquid assembled at the surface of a bubble since overall free energy was minimized with these particles adsorbed onto the gas-liquid interface. They derived theoretically the conditions under which a layer of particles could stabilize bubbles against dissolution into liquid at zero or negative capillary pressure.

Following the indication of the theoretical work of Kam and Rossen [35], Du et al. [36] investigated experimentally whether particles partly wetted by both gas and liquid could form a shell which was rigid enough to prevent bubble from shrinking due to disproportionation. Disproportionation is a effect that the net diffusion flux from small bubbles to large ones due to the greater Laplace pressure of the former. They observed that bubbles stabilized by partially hydrophobic silica nanoparticles were stable to disproportionation for a few days, comparing with similar bubbles formed by proteins, which typically dissolved in 1 or 2 hours. The phenomena that some bubbles shrank before the bubble radius became constant suggested that some rearrangement and/or optimal packing of the particles at the bubble surface might occur during the shrinkage, leading to a denser layer with very little space between particles. Additional experiments were performed by Dickinson et al. [37] to explore how variations in aggregation and hydrophobicity of silica particles affected formation and stability of bubbles. They concluded that the formation and stability of bubbles covered with particles depended on a balance between the tendency of the particles to aggregate and their tendency to adsorb onto the bubble surface. Extensively aggregated particles could not adsorb quickly enough to form stable bubbles. They suggested that the stability might be caused by the formation of a continuous network of particles at the bubble surface.

Kostakis et al. [38] explored the effect of a wider range of salt concentrations and the electrolyte valency on the stability of bubble covered by partially hydrophobic silica particles. They observed the stability of the bubbles to disproportionation increased with an increasing NaCl concentration from 0.5 to 3 mol dm⁻³. While the use of CaCl₂ and Al(NO₃)₃ at similar ionic strengths could not form bubbles with equivalent stability. They concluded that the enhanced stability was not merely due to

increased screening of electrostatic repulsion. Rather, addition of salt increased the effective hydrophobicity of the particles in some way as demonstrated by contact-angle measurement of water droplets on the silica. Through rheological measurements, they observed an increasing salt concentration in this range also resulted in the formation of weak particle gels, which suggested the formation of such networks might be an important part of the mechanism of enhanced bubble stability.

Alargova et al. [39] studied bubbles stabilized solely by hydrophobic polymer microrods whose length was several tens of micrometers and diameter was less than 1 μm . The contact angle of the polymer rods and water was estimated to be between 80° and 90° corresponding to intermediate hydrophobicity. They observed the bubble was densely covered by a thick layer of intertwined polymer rods. They concluded superstabilization of the bubbles was due to the mechanical rigidity of the continuous net of overlapping and entangled microrods at the bubble surface and the strong adsorption of the polymer rods on the air-water interface. In contrast, Binks and Horozov [40] reported hydrophilic silica particles with a surface content of SiOH of 62%, 51% and 42% were unable to form stable bubbles.

Abkarian et al. [41] addressed the mechanism of stabilization by both experimental and numerical methods. They observed that bubbles coated by polystyrene particles of uniform size gradually developed faceted polyhedral shapes which provided stability against dissolution in air-saturated water. Polystyrene particles adsorbed on a partially coated bubble carried out Brownian motion shown in Figure 1.4a. And Brownian motion of the particles was arrested when the interparticle distances became smaller as gas dissolved in liquid. Further dissolution made the bubble deformed away from a spherical shape before stabilizing. The final nonspherical shape depended on the ratio of the particles' radius and bubble's radius. Bubbles with ratio much smaller than 0.1

appeared crumpled (Figure 1.4b). Crumpled shapes were also reported by Ramsden [42], Binks and Horozov [40], and Xu et al. [43]. While faceted polyhedral structures were observed for bubbles with ratio around 0.1 (Figure 1.4c). Through SURFACE EVOLVER simulations, they concluded that the faceted state had a minimum energy with a mostly saddle shaped air-water interface which had zero mean curvature. The vanishing of Laplace overpressure was the mechanism that arrested dissolution and stabilized the bubbles.

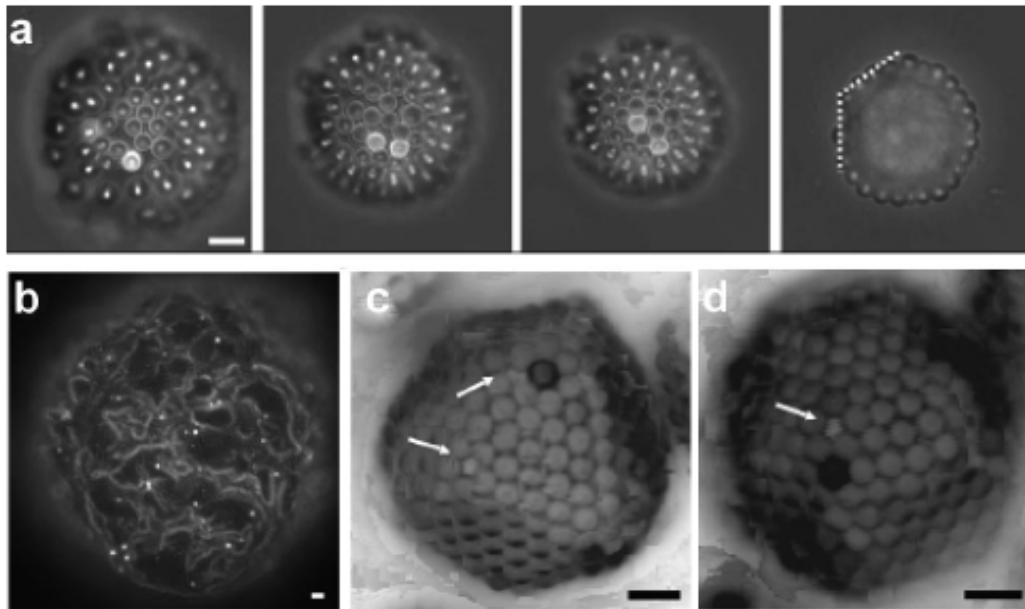


Figure 1.4: (a) Experimental pictures of dissolution of a partially coated bubble, 3 s between each picture. Distances between particles were reduced and the bubble developed planar facets gradually as gas dissolved into liquid (white dashed lines). (b)–(d) A few stable crumpled and faceted shapes of bubbles, the ratio a/R : (b) 0.008, (c) 0.19, (d) 0.22. The white arrows pointed out missing particle defects at the vertices of the bubble. Bubble shapes like these remained intact for days if not longer. Scale bars were $8 \mu\text{m}$. Taken from ref. [41].

Although the mechanism by which bubbles covered by solid particles are stable to dissolution is not yet fully understood, the brief review presented suggests some general trends and concepts: (I) It is essential to have particles adsorbed at the bubble surface before any stabilization can take place; thus the particles have to be partly wetted by both air and water. (II) The formation of a continuous network of particles at the bubble surface is of fundamental importance to the stability of bubbles. (III) The stability of bubbles is linked with the particle configuration and the equilibrium shape of the fluid-fluid interface.

1.7 Applications of bubbles driven by a sound field

Bubbles in liquids driven by a sound field are used in many disciplines: for example, they clean surfaces [44] in ultrasonic water baths, and they catalyze unique chemical reactions in sonochemistry [45, 46]. Shelled micrometer sized bubbles reflect diagnostic ultrasound [47] and allow pictures of organ perfusion [48] or cancerous tumors [49] to be taken. Such shelled microbubbles have the advantage of being stable in the body for a sufficient time in comparison with the ultrasonic contrast agent of just gas suspended in liquid, which is unstable in the blood stream and can not allow enough imaging time [50]. Recently, bubbles have been engineered to bind to certain cell types [51], to deliver medication, to serve as a viral surrogate for gene therapy [52].

1.8 A guide through the chapters

In Chapter 2 we describe the procedure for fabricating stable magnetic microspheres by self-assembly of magnetic nanoparticles at the oil-water interface. And we present the measurements of magnetophoretic velocities of individual magnetic microspheres with oil droplets coated by magnetic nanoparticles in a defined magnetic field in order to investigate the magnetic properties of such microspheres.

In Chapter 3 we present a liquid-liquid microfluidic system for transporting millimeter-sized oil droplets covered with magnetic microparticles, which float freely at the air-water interface and are driven by a magnetic field generated by a pair of electromagnetic coils. To study how the distance between the tips of electromagnetic coils and the water surface, the driving electric currents, as well as the sizes of oil droplets affect the transport time of oil droplets, we measure the average velocities of individual oil droplets transported between the two tips by varying each parameter systematically.

In Chapter 4 we describe the procedure for creating a new type of bubble that has a permanent magnetization by self-assembly of magnetic nanoparticles at the air-water interface. To study the compressibility of the magnetic shell, a single magnetic bubble is exposed to an acoustic field and its radial response is recorded with a high speed camera. The magnetic properties of these bubbles are measured by fitting the trajectory of individual bubbles in a magnetic field to a force balance model.

The impact of a magnetic bubble's volume oscillation on its mean rise velocity which is studied by measuring the mean rise velocity once without and once with the acoustic field is investigated in Chapter 5.

The main results of our studies on magnetic oil droplets and magnetic bubbles as well as future work are summarized and discussed in Chapter 6.

Chapter 2

Magnetophoresis of microspheres covered by magnetic nanoparticles

2.1 Introduction

It has been well established that fine solid particles with proper hydrophobicity can spontaneously adsorb onto the oil-water interface [1]. Energy is required to remove the particle to the oil phase or to the water phase since adsorption is energetically favored. This mechanism has been used to create Pickering emulsions [3], which are stabilized by fine particles at the oil-water interface [53, 54], and to fabricate colloidosomes by the self-assembly of fine particles onto the interface of emulsion droplets. Recently, colloidosomes have been recognized as promising potential vehicles due to the possibility to precisely control their size, permeability, mechanical strength and compatibility [1]. Also magnetic colloidosomes have gained interest since they can be manipulated with external magnetic fields, and may therefore be used in targeted delivery [15].

The magnetic properties of magnetic particles rely on many factors, such as the shape of the particles, its microstructure, and the type, amount and distribution of magnetic material within particles; thus their properties may strongly differ [20]. Detailed knowledge of the properties of individual magnetic particles is required by an increasing number of biomedical applications ranging from microfluidic

applications in lab-on-a-chip system to drug delivery [21]. The magnetic characterization of individual micrometer-sized solid magnetic particles has been done by magnetophoretic analysis [20], while submicron particles have been studied using particle tracking of thermally fluctuating particles placed in a potential well [21]. Here we present a method for fabricating such colloids by self-assembly of magnetic nanoparticles onto the interface of emulsion droplets. Such micrometer-sized oil droplets encapsulated by a shell composed of magnetic nanoparticles have so far not been characterized using magnetophoresis. We investigate the motion of individual magnetic microspheres in a defined magnetic field gradient, estimate the susceptibilities of individual magnetic microspheres, and show that the magnetic moment of the oil droplets scales with their diameters.

2.2 Experimental methods

2.2.1 Materials

All chemicals were used as received without further purification. Iron (II) chloride tetrahydrate ($\text{FeCl}_2 \times 4\text{H}_2\text{O}$ 99%), Potassium hydroxide (KOH, volumetric standard, 1.0 M solution in water) and hydrogen peroxide (H_2O_2 , 3 wt. % solution in water) were purchased from Aldrich, whereas n-hexadecane ($\text{C}_{16}\text{H}_{34}$, 99%) was purchased from Acros and bovine serum albumin (BSA) was purchased from Sigma. Sodium dodecyl sulfate (SDS, electrophoresis grade) was purchased from Fisher. Ultrapure water was used to prepare the aqueous solutions.

2.2.2 Preparation of magnetic nanoparticles

Magnetite nanoparticles were prepared in open air at room temperature [55]. We added 4.2 mL of 1 M KOH aqueous solution to 25 mL of 0.1 M FeCl_2 aqueous solution. Then 250 μL of H_2O_2 3 wt. % aqueous solution was added into the solution to yield a black precipitate which was strongly attracted to a permanent magnet. The particles were separated by magnetic decantation, washed with 3×20 mL distilled water and 2×20 mL acetone, and finally dried in air at room temperature. As reported in Ref. [11], the spinel structure of the nanoparticles is an intermediate between Fe_3O_4 and $\gamma\text{-Fe}_2\text{O}_3$.

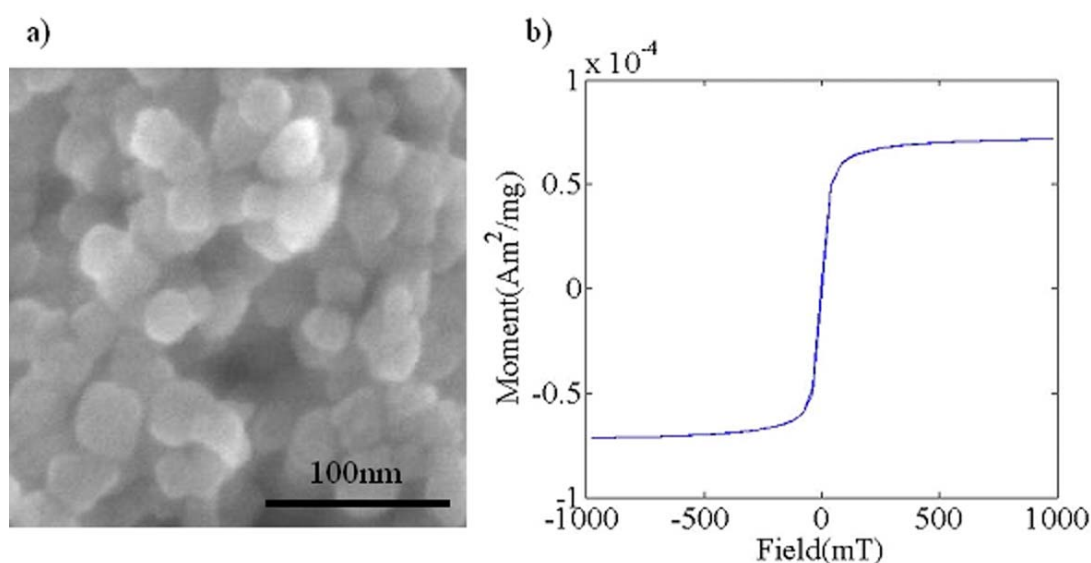


Figure 2.1: (a) The SEM image of magnetic nanoparticles ranging in size from 16 to 44 nm with an average diameter of $d = 29 \pm 6$ nm (b) Magnetic moment versus magnetic field measured for powder of magnetic nanoparticles.

Figure 2.1a shows a scanning electron microscope (SEM) image of the magnetic nanoparticles. Image analysis revealed that the particles have irregular shape and are polydisperse in size ranging from 16 to 44 nm with an average diameter of $d = 29 \pm 6$ nm. The magnetic properties of the nanoparticles were measured using a vibrating sample magnetometer (Lakeshore 7404). The anhysteretic curve of magnetic moment versus magnetic field is shown in Figure 2.1b.

2.2.3 Preparation of magnetic microspheres

An amount of 3 mg of magnetic nanoparticles was washed with 1 mL ultrapure water once, dispersed in 1 mL ultrapure water, and sonicated for one minute to get a uniform black suspension by the sonicator (DH.D250H). Next 15 μ L of 5 mM of the surfactant SDS was added to the solution and shaken by hand for one minute, followed by sonication for one minute. We then added 400 μ L of the oil hexadecane and shook the container by hand for 3 minutes, followed by sonication for one minute to form magnetic microspheres. The surfactant SDS will cover the oil droplets, and also assist in the attachment of magnetic nanoparticles to the oil droplets. Three phases were distributed in the container due to their different densities. The lower phase was water; oil droplets coated with magnetic nanoparticles were in the middle layer, while the upper phase was hexadecane. The microspheres are very stable over time and maintain their appearance for over 7 months.

The experimental setup used for magnetophoretic measurements is shown in Figure 2.2. We use a glass slide partially covered with Teflon having a glass well with a diameter of 8 mm as a sample holder for the liquid containing magnetic microspheres.

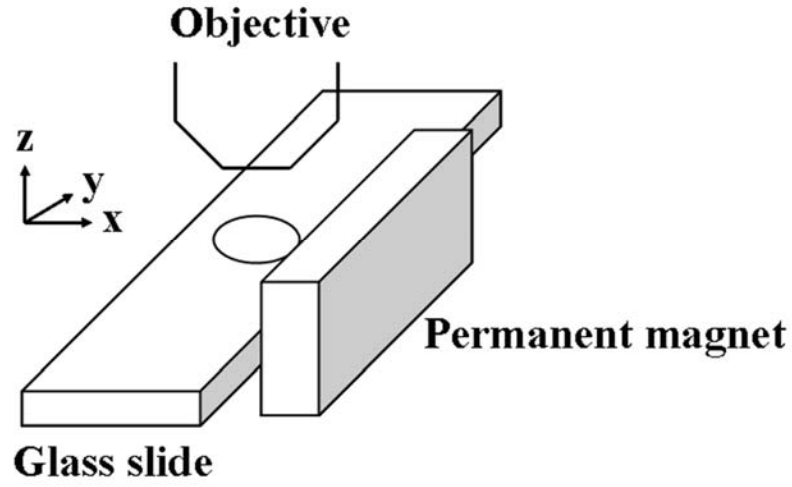


Figure 2.2: Experimental devices for magnetophoretic measurements.

Then a cover glass of size $18 \times 18 \text{ mm}^2$ is put on top of the well, thus forming a cell of thickness around 0.1 mm. The magnetic microspheres move towards the permanent magnet fixed relative to $50\times$ microscope objective, while the motion is observed with a Leica polarization microscope ($50\times$ microscope objective) used in transmission mode and recorded with a CCD camera (25 fps). The pixel size in a movie is $0.3 \text{ }\mu\text{m}$. The recorded movies are analyzed manually. The magnetic field is measured using a Gaussmeter with a Hall Effect probe (GM04, Hirst Magnetic Instruments Ltd., UK). The distance between the center of the objective and the front surface of the magnet is 14.5 mm so that an object at the center of the picture captured is 14.5 mm away from the magnet. The dimension of the picture typically is $188 \text{ }\mu\text{m} \times 149 \text{ }\mu\text{m}$. We measure the magnetic field at the distance of 14 mm away from the magnet B_1 and at the distance of 15 mm away from the magnet B_2 . The average magnetic field is $B = (B_1 +$

$B_2)/2 = 24.7$ mT and the average field gradient is determined as $(B_1 - B_2)/1$ mm = 2.9 mT/mm. Although this region is larger than the area of the picture, their centers coincide and the magnetic field decreases almost linearly in the region from 14 mm to 15 mm away from the magnet. The error caused by using the average magnetic field of 24.7 mT as the average magnetic field in the area of the picture is less than 0.1 mT. An amount of 2 μ L of the magnetic microspheres in the middle layer was dissolved in 1 mL of 1 mg/L BSA solution as the sample which was used for magnetophoretic measurements. By using BSA we could prevent magnetic microspheres from being adsorbed to the glass slide. It is known that BSA has an effective negative charge at pH = 7 [56], thus adsorbing to the positively charged nanoparticles and preventing them from adsorbing to the negatively charged glass slide.

2.3 Results

In order to understand how the magnetic microspheres can be transported, we did magnetophoretic measurements of the individual magnetic microspheres. A typical magnetophoretic behavior of a magnetic microsphere is shown in Figure 2.3, which was made by superimposing captured images at 5 s intervals. The x component of the velocity of the microsphere was measured from the superimposed images.

The x components of the velocities in magnetic field $B \approx 24.7$ mT, $dB/dx \approx 2.9$ mT/mm for 30 microspheres which appeared to be uniformly coated with magnetic nanoparticles are plotted against their radii in Figure 2.4. This figure shows that larger microspheres usually have larger velocities, typically up to 10 μ m/s. However, it is also clear that microspheres of the same size can have velocities differing by a factor

of 4 or larger. We also measured the x -component of the velocities of microspheres which had clusters attached to their surfaces, and found that their velocities had a larger value, with a maximum of approximately $70 \mu\text{m/s}$.

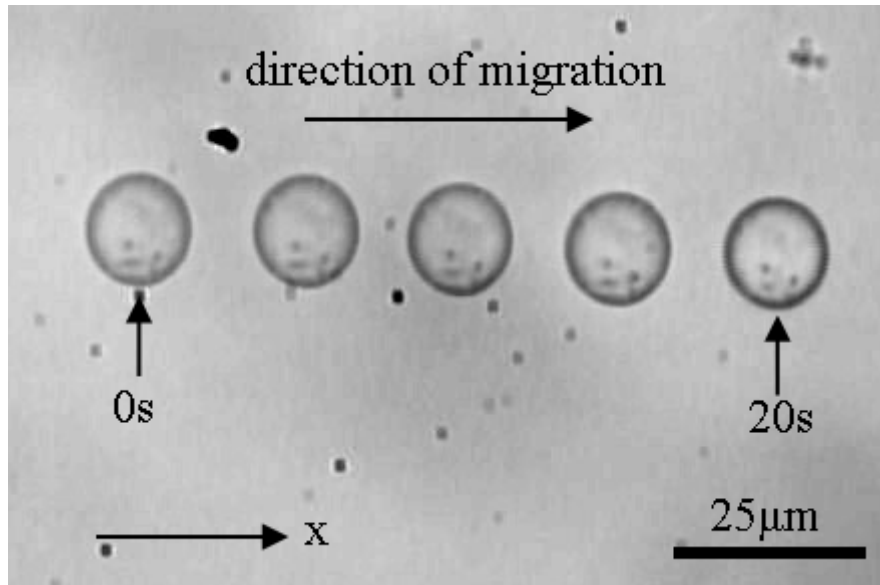


Figure 2.3: The magnetophoretic behavior of a single magnetic microsphere in magnetic field $B = 24.7 \text{ mT}$, $\partial B / \partial x = 2.9 \text{ mT/mm}$. This microphotograph was made by superimposing the images captured at 5 s intervals.

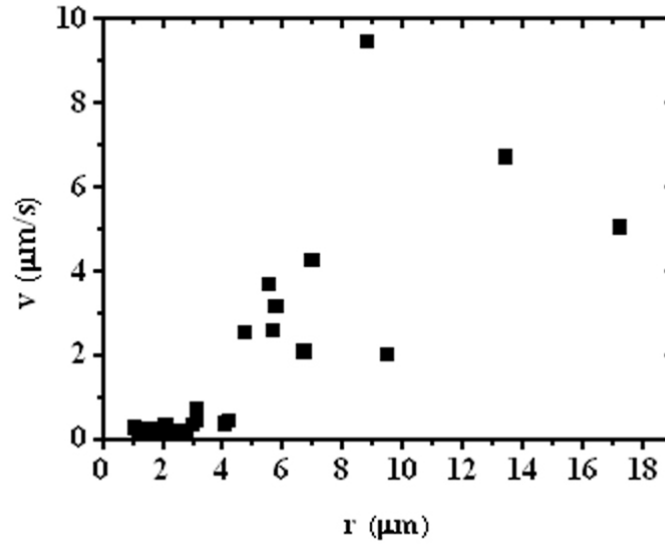


Figure 2.4: Diagram of the x component of the velocities under magnetic field $B \approx 24.7$ mT, $dB/dx \approx 2.9$ mT/mm for 30 microspheres which appeared to be coated with magnetic nanoparticles uniformly in the images versus their radii. $\Delta r = 0.3$ μm and The errors of the velocities are comparable to the size of the squares with the upper bound $\Delta v = 0.3$ $\mu\text{m/s}$. The error of the velocity is estimated using the expression $\Delta v = \left| \frac{\Delta s}{t} \right| + \left| \frac{s}{t^2} \Delta t \right|$, where s is the distance traveled by the microsphere in the time interval t , Δs is equal to 0.3 μm , and Δt is equal to 0.04 s which is confined by the speed of the camera (25 frames per second).

2.4 Discussion

The x -component of the magnetic force F_{mx} acting on the magnetic microsphere in a magnetic field can be expressed as [57-59]

$$F_{mx} = \frac{\chi_{sphere}}{\mu_0} B \frac{\partial B}{\partial x}, \quad (2.1)$$

where χ_{sphere} is the susceptibility of the microsphere, B is the magnetic field in the absence of the microsphere, and μ_0 is the vacuum magnetic permeability. Here we assume that the medium is nonmagnetic and the magnetic microsphere is paramagnetic.

In the experiments, a nearly linear relation exists between the magnetic moment of magnetic nanoparticles and the magnetic field when absolute value of the magnetic field is less than 40.9 mT shown in Figure 2.1, while the magnetophoretic measurements were conducted in this region ($B \approx 24.7$ mT). The susceptibility of the medium (1 mg/L BSA solution) is negligible (-7×10^{-7}) compared with that of magnetic nanoparticles (8×10^{-3}). Therefore Eq. (2.1) is a good approximation for the magnetic microspheres.

In our experiment we observed that the diameters $2r$ and velocities v of the spherical oil droplets ranged between $2\mu m < 2r < 36\mu m$, $0.06\mu m/s < v < 10\mu m/s$, respectively. From these data we calculated Reynolds number to be in the range $Re < 4 \times 10^{-4} \ll 1$. For this reason the viscous drag force acts on the microsphere F_{Dx} can be represented through Stokes' drag law [22, 60]

$$F_{Dx} = -6\pi\eta r v_x, \quad (2.2)$$

where η is the dynamic viscosity of the liquid and v_x is the magnetophoretic velocity of the microsphere in the x -direction and r is the radius of the microsphere. Equations (2.1) and (2.2) can be combined with Newton's 2nd law

$$F_{mx} + F_{Dx} = m a_x, \quad (2.3)$$

where a_x and m are the acceleration and the mass of the microsphere, respectively. Since the mass and Reynolds numbers are small, the inertia ma_x is also negligibly small, thus allowing us to represent χ_{sphere} as

$$\chi_{sphere} = \frac{6\pi\eta\mu_0rv_x}{B\frac{\partial B}{\partial x}}. \quad (2.4)$$

Equation (2.4) allows us to calculate χ_{sphere} using the measured velocity v_x and r . The values of χ_{sphere} of 30 microspheres are shown in Figure 2.5. These microspheres are fabricated by self-assembly of magnetic nanoparticles at the surface of oil droplets; thus they have a spherical magnetic shell. The susceptibility of a spherical shell is $\chi_{sphere} = V_{shell}f(\chi_m)$ [61], where V_{shell} is its volume, χ_m is the dimensionless susceptibility of the magnetic nanoparticles and $f(\chi_m)$ is a function of the dimensionless susceptibility χ_m . V_{shell} is equal to the surface area of the microsphere multiplied by the thickness of the shell which is unknown. Therefore χ_{sphere} is proportional to the surface area of the microsphere multiplied by the thickness of the shell. The red line of $\chi_{sphere} = 1.13 \times 10^{-7} \times r^2 \text{ m}^3$ in Figure 2.5 was fitted by a least-square method. Considering the surface area of a microsphere $4\pi r^2$, the curve of $\chi_{sphere} = 4\pi r^2 A$ ($A = 1.13 \times 10^{-7}/4\pi \text{ m}$) suggests that χ_{sphere} is roughly proportional to the surface area of the microspheres and different microspheres have different thickness of the shell. This is reasonable since the magnetic nanoparticles assemble to the surface of the oil droplet, which means the larger the surface area, the more opportunities for the magnetic nanoparticles to attach to the surface. However, it is also clear that microspheres of the same size can have susceptibilities that differ by more than a factor of 4. An explanation for this variation of susceptibilities could be

the number of magnetic nanoparticles attached to the surface of oil droplets, distribution of magnetic nanoparticles on the microspheres and the strong differences between individual magnetic nanoparticles due to the shape of the nanoparticles and their nanostructure [21].

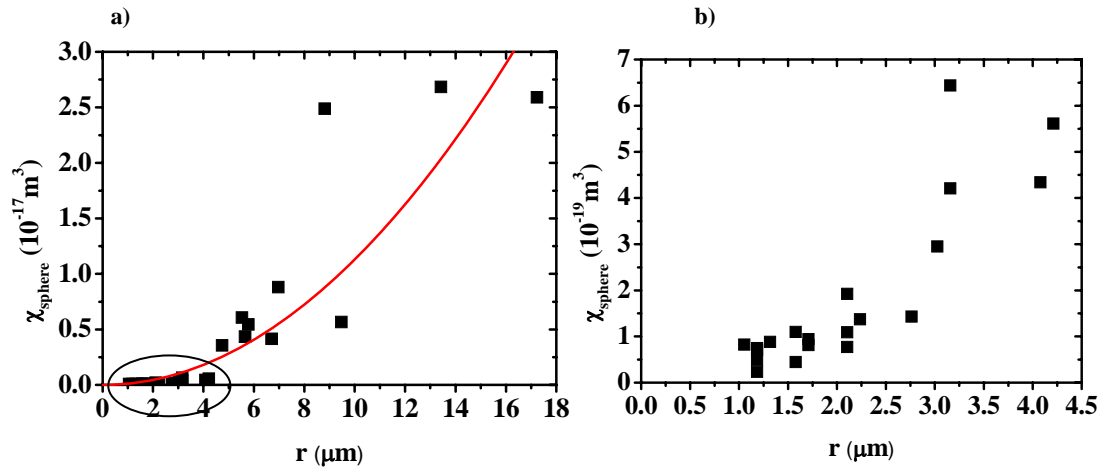


Figure 2.5: (a) The susceptibility of individual magnetic microspheres calculated according to the equation (2.4) versus the radius. (b) The data in the circled region of part (a). The red line of $\chi_{\text{sphere}} = 1.13 \times 10^{-7} \times r^2 \text{ m}^3$ was obtained by a least-square method. According to equation (2.4),

the error of χ_{sphere} can be calculated by the expression
$$\Delta \chi_{\text{sphere}} = \frac{6\pi\eta\mu_0}{B \frac{\partial B}{\partial x}} (|\Delta r v_x| + |r \Delta v_x|)$$

considering the error of velocity and the error of radius measurement as the main sources of error.

$\Delta \chi_{\text{sphere}}$ is a function of r and v_x , being comparable to the size of the squares for the data in part (b) and less than 8% for the other data in part (a).

For a magnetic field of 24.7 mT, we calculated the average magnetic moment of one nanoparticle to be $m_l = 1.96 \times 10^{-18} \text{ A} \cdot \text{m}^2$, see Figure 2.1b. So the number n of nanoparticles attached to the surface of the oil droplets can be estimated by

$$n = \frac{\chi_{\text{sphere}} B}{\mu_0 m_l} . \quad (2.5)$$

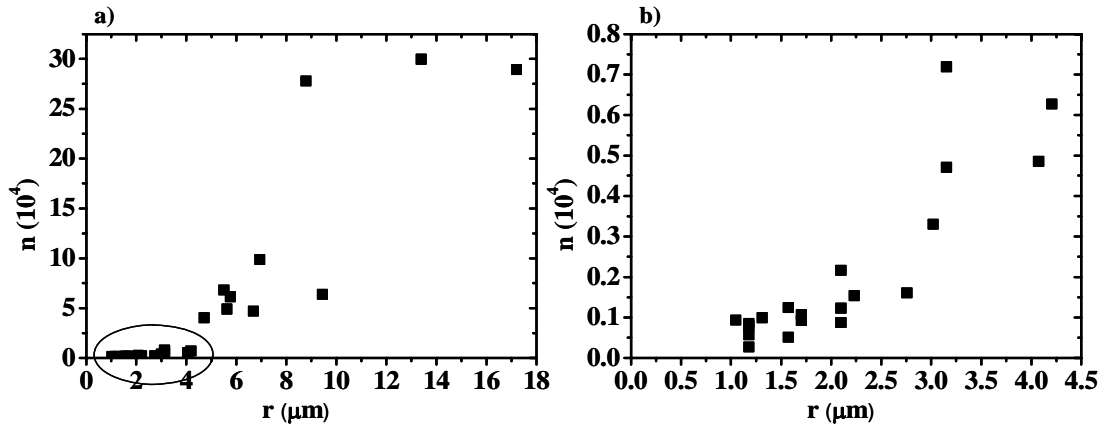


Figure 2.6: The number of the magnetic nanoparticles per oil droplet versus the radius of the oil droplets for 30 microspheres. Figure b is magnified one of the circled part of Figure a.

Figure 2.6 shows the number of the magnetic nanoparticles per oil droplet versus the radius of the oil droplets for 30 droplets. When the nanoparticles are close-packed on the surface of the oil droplets, the number of the particles per oil droplet is given by

$$n_0 = \frac{4\pi r^2}{\pi d^2} , \quad (2.6)$$

where d is the average diameter of the magnetic nanoparticles. We define

$$R = \frac{n}{n_0} . \quad (2.7)$$

Here R is a measure of how large fraction of the oil droplets is coated with magnetic nanoparticles. Diagram of ratio of number R of the oil droplets versus the radius for 30 oil droplets is shown in Figure 2.7. R is in the range of 1% to 19%. The microspheres of the same size have strong difference in surface coverage of magnetic nanoparticles. This result suggests that the difference in the number of magnetic nanoparticles attached to the oil droplets is the main reason for the variation in magnetic susceptibilities of microspheres with the same size.

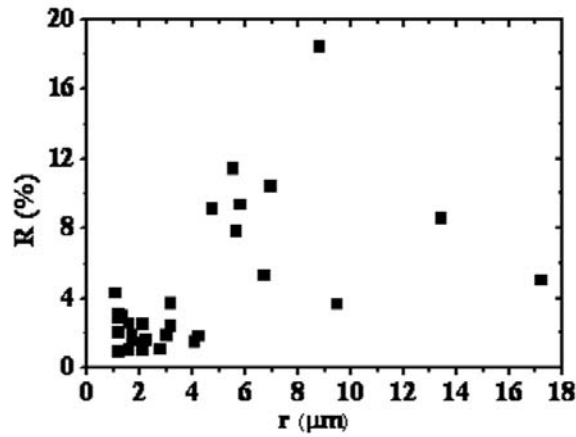


Figure 2.7: Diagram of the surface coverage of oil droplets by magnetic nanoparticles R versus the droplet's radius for 30 oil droplets.

It should be noted that there is a gap between the microspheres and the glass slides due to electrostatic repulsive force, thus the microspheres can move smoothly in the magnetic field without rotation. However the exact distances between the microspheres and the upper cover glass slide or lower glass slide are unknown. We use the expression $F_{Dx} = -6\pi\eta r v_x$ to estimate the drag force on the microspheres which are confined between two glass slides. This causes errors since $F_{Dx} = -6\pi\eta r v_x$ is valid in an unbounded liquid and the microspheres experience wall effects due to the glass slides. Wall-corrected drag force acting on the sphere which moves without rotation parallel to two stationary walls can be written as $F_w = F_{Dx} \times J$ [62]. J is a function of the sphere position, sphere radius and wall-to-wall spacing. For example, in our experiments the wall-to-wall spacing is around 0.1 mm and the biggest sphere radius is 18 μm . If the distance of the upper glass slide and the center of the microsphere is 1.8 μm , J is approximately 2.4 [62]. If the distance is smaller than 1.8 μm , J becomes even larger. This large error caused by the uncertainty of the distances between the microspheres and glass slides also influences our estimation of the magnetic susceptibility and the surface coverage of the microspheres.

2.5 Conclusion

We fabricated magnetic microspheres by self assembly of magnetic nanoparticles onto the interface of emulsion droplets and measured the magnetophoretic velocities of this kind of magnetic microspheres in a defined magnetic field. We found that larger microspheres usually have larger velocities. However, it is also clear that microspheres of the same size can have velocities that differ by more than a factor of

4. Susceptibilities of 2-35 μm magnetic microspheres have been calculated to characterize their magnetic properties. We found that larger microspheres usually have a larger susceptibility and χ_{sphere} is proportional to the surface area of the microsphere roughly. However, it is also clear that microspheres of the same size can have susceptibilities which differ by more than a factor of 4. Since many drugs can be dissolved in the oil phase and the magnetic microspheres are stable and controlled efficiently by an external magnetic field, we hope the current study can assist efforts towards obtaining a tool for controlled drug delivery.

Chapter 3

Transport of free-floating droplets using electromagnetic coils

3.1 Introduction

‘Lab-on-a-chip’ systems which integrate single or multiple laboratory functions on a single chip with sizes from millimeters to a few centimeters provide interesting tool set for genomics applications, bio-analysis and medical diagnostics. Low internal chip volumes are beneficial for lower costs of expensive reagents and less volume of sample fluid. Transport of small volumes of liquid containing the required material is an important task in the microfluidic systems with permanently rigid channels, pumps and valves [32]. The microfluidic systems which allow liquid to be transported as droplets on a solid surface are more flexible than the continuous-flow based microfluidic devices. However, both of these systems suffer from similar problems that material such as DNA may adhere to the walls since the liquid is in contact with the solid surface [30].

Several actuation mechanisms have been developed in the past to transport small droplets, including the use of thermalcapillary effect [24, 25], surface chemical gradients [26], light [27], electrostatic actuation [28], electrowetting [29], dielectrophoretic force [30], and magnetism [31-34].

Magnetic actuation is another interesting option which has little influence on the non-magnetic samples [32, 33, 63]. However it requires introducing magnetic material into the droplet. Recently, magnetic microparticles and nanoparticles have been dispersed in the small droplets as actuators to transport droplets on the solid surface using planar microcoils [32, 33, 64-66]. Here we describe a liquid-liquid microfluidic system for transporting millimeter-sized spherical oil droplets coated with paramagnetic microparticles, which float freely at the air-water interface and are driven by a magnetic field gradient applied by a pair of electromagnetic coils above the surface of the water phase. Material can be dispersed inside oil droplets and the influence on it can be minimized since magnetic colloids, the surface of which can be modified with certain functional groups, are located on the surface of droplets.

3.2 Experimental methods

A schematic drawing of the experimental setup is shown in Figure 3.1. Two identical electromagnetic coils are fabricated by winding a 0.75 mm diameter copper wire around a 2.44 mm diameter soft ferromagnetic rod with a tip of length 3.70 mm. The winding design consists of three coil layers with around 36 turns each. We measured z component of the magnetic field at the point 1.1 mm below tip 1 using a Gaussmeter with a Hall Effect probe (GM04, Hirst Magnetic Instruments Ltd., UK) shown in Figure 3.2. The best linear fit of $B_z = \alpha I + \beta$, where $\alpha = 9.9$ mT/A and $\beta = 6.4$ mT, suggests that the magnetic field of the coil is proportional to the driving current. The oil droplets migrate to the tip when the electric current is supplied to the corresponding coil and hover below it, trapped by the field gradient. When no electric

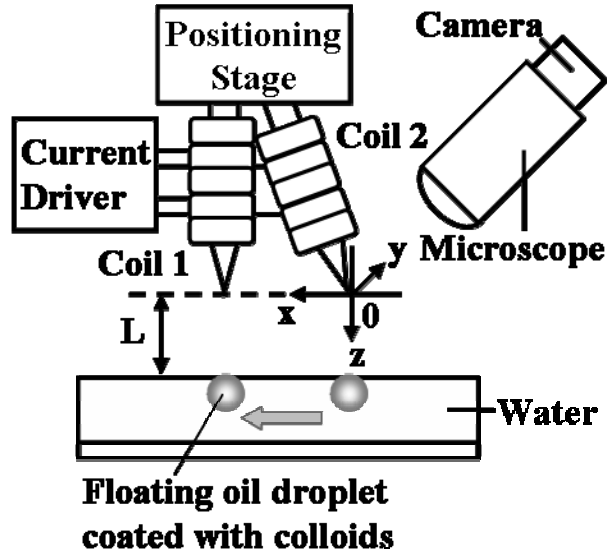


Figure 3.1: Schematic diagram of the oil droplet transport system.

current is supplied to the coils, the magnetic force acting on droplets is too weak to move them, and we found that the magnetic tip remanence does not play an important role when the current is sufficiently large. The oil droplets are readily moved between two fixed positions by switching off the current of the related coil. The motion of oil droplets is recorded with a CCD camera mounted on a optical microscope, where the objective lens is mounted on a mechanical stage and making an angle of about 45° with the water surface. In order to calibrate the measured lengths taking into account geometrical distortions we used an object of known dimensions. We measured the diameters of oil droplets using another setup with higher accuracy. A microscope objective ($5\times$) of a Leica polarization microscope is at an angle of 90° with the water surface so that there is no distortion in the images of oil droplets. The diameters of oil

droplets were obtained by detecting the contours. Each pixel represents 1 μm . And the error of diameter measurements is estimated as 5 μm .

The coordinates of the system are selected as shown in Figure 3.1. The origin is at the center position of the oil droplet which hovers below tip 2 of the electromagnetic coil 2 when electric current is supplied to it. The configuration of the system has an advantage that the heat produced by the peak current of 2.5 A used in the coils with a resistance of 0.34 Ω can not affect the system due to the air gap of $L \approx 1 \text{ mm}$ between tips and the water surface.

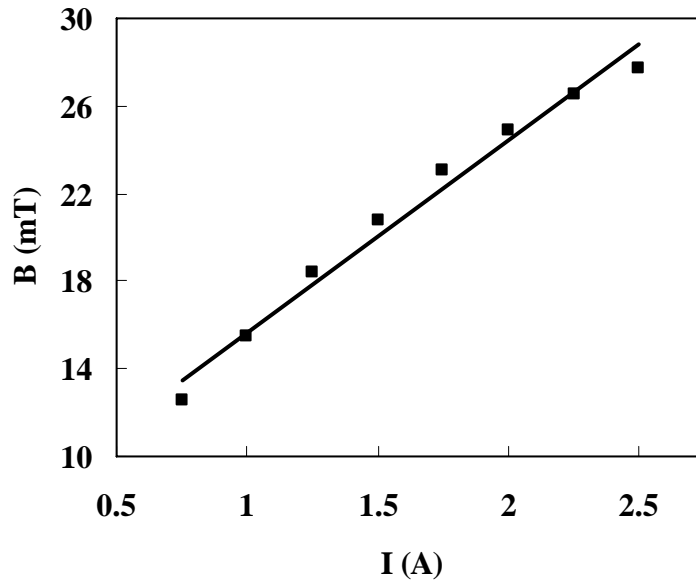


Figure 3.2: The z component of the magnetic field at the point 1.1 mm below tip 1 versus the driving current in coil 1. The solid line is the best linear fit: $B_z = \alpha I + \beta$, where $\alpha = 9.9 \text{ mT/A}$ and $\beta = 6.4 \text{ mT}$. The accuracy of the magnetic field measurement is $\pm 0.1 \text{ mT}$ and the accuracy of the current is $\pm 0.01 \text{ A}$.

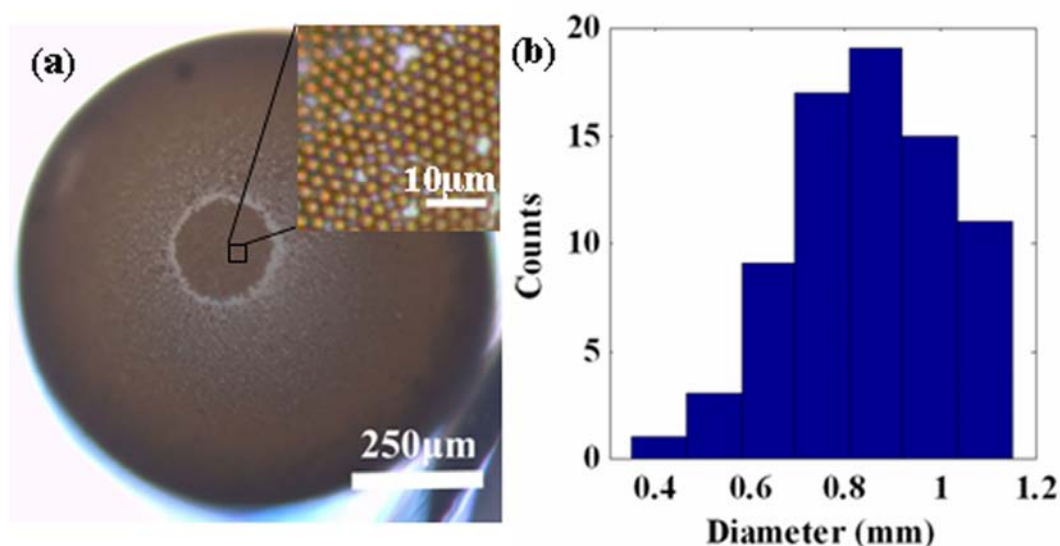


Figure 3.3: (a) An optical image of an oil droplet coated with paramagnetic colloids floating at the air-water interface. The inset shows the monolayer structure of paramagnetic colloids in situ taken with a Leica polarization microscope at a higher magnification (50× microscope objective). (b) Histogram of the size-distribution for 75 oil droplets.

Oil droplets coated with paramagnetic colloids are formed by self-assembly of colloids at the oil-water interface [1, 53], see Figure 3.3a. The oil is n-hexadecane ($C_{16}H_{34}$, 99%) of density 773 kg/m^3 purchased from Acros and paramagnetic colloids of radius $1.4 \pm 0.2 \text{ } \mu\text{m}$, density $1.6 \times 10^3 \text{ kg/m}^3$ were purchased from Dynal. These particles are composed of highly cross-linked polystyrene with nanoscale superparamagnetic particles ($\gamma\text{Fe}_2\text{O}_3$ and Fe_3O_4) precipitated in pores distributed throughout the particles and their surfaces are modified with NH_2 groups. The paramagnetic colloids are supplied at a density of 2×10^9 beads/mL, and were rinsed by magnetic decantation 5 times in ultrapure water before use. We mixed 50 μL of beads in 500 μL of ultrapure water to obtain a uniform suspension, and thereafter

added 200 μL of hexadecane into the suspension. Upon vigorous shaking (by hand), microscopic hexadecane droplets were formed, and the brown colloids attached to these droplets. After only a few seconds the oil droplets coated with colloids floated to the top of the water phase due to the lower density of hexadecane.

3.3 Results and discussion

The size distribution of these oil droplets (Figure 3.3b) are in the narrow range from 0.456 ± 0.005 mm to 1.177 ± 0.005 mm. Oil droplets coated with magnetic colloids float at the air-water interface due to their low mass density and keep spherical with a small fraction of their top compressed to form a nearly two dimensional hexagonal close-packed structure at the air-water interface, see Figure 3.3a. The ring at the top of the droplet is the oil-air-water three phase contact line.

In order to characterize the system, we investigated how the distance L between the tips and the water surface as well as the driving electric currents I affect the transport of oil droplets. The distance L was first fixed and then one oil droplet was trapped using coil 2 fed with a constant current. We then turned on the current in coil 1, and thereafter turned off the current in coil 2, thus causing the droplet to move from tip 2 to tip 1 and hover below it. Next we changed L and I , respectively, and conducted a series of experiments. An example of a recorded image sequence from such experiments is shown in Figure 3.4. The center position of the droplet is obtained from the recorded images. The initial position of the droplet at time t_1 is (x_1, y_1) and its final position at time t_2 is (x_2, y_2) . The displacement is calculated as $\sqrt{(x_1 - x_2)^2 + (y_1 - y_2)^2}$ and the average velocity is calculated as

$\sqrt{(x_1 - x_2)^2 + (y_1 - y_2)^2} / (t_2 - t_1)$. Figure 3.5a shows the trajectory of an oil droplet with a diameter of 0.921 ± 0.005 mm ($L = 1.1 \pm 0.1$ mm). The filled squares and the open squares are the results for $I = 1.5$ A and $I = 2.5$ A, respectively. The fitted curves show that the one-dimensional motion of the oil droplet can be modeled assuming a constant acceleration a . Figure 3.5b shows the average velocity of an oil droplet with a diameter of 0.656 ± 0.005 mm versus L for $I = 1.5$ A, 2 A, and 2.5 A. It can be seen that the average velocity of the oil droplet decreases linearly with L . When L changes from 0.2 mm to 1.9 mm, the average velocity increases by more than 2.6 times. Figure 3.5c shows the average velocity of oil droplets of different diameters as a function of I for $L = 1.1 \pm 0.1$ mm. The average velocity of the oil droplets increases linearly with I since a larger current leads to a larger magnetic field and field gradient.

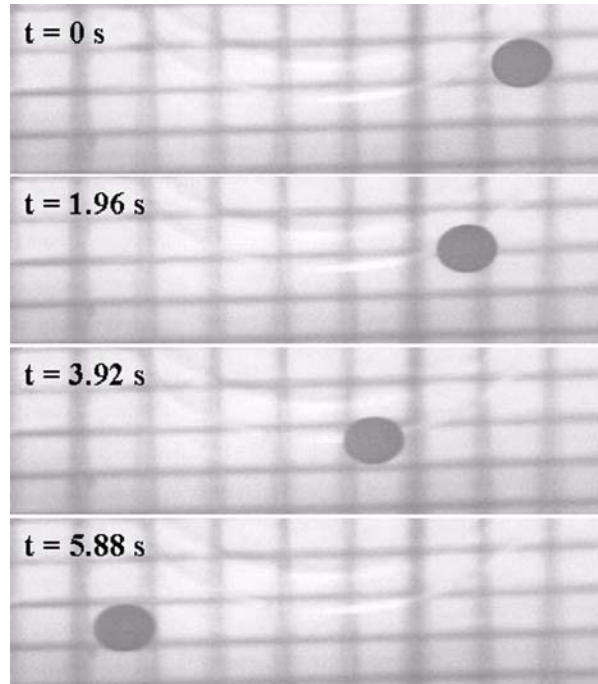


Figure 3.4: Sequence of four images demonstrating the transport of an oil droplet with a diameter of 0.921 ± 0.005 mm from tip 2 to tip 1 when $L = 1.1 \pm 0.1$ mm and $I = 0.75$ A.

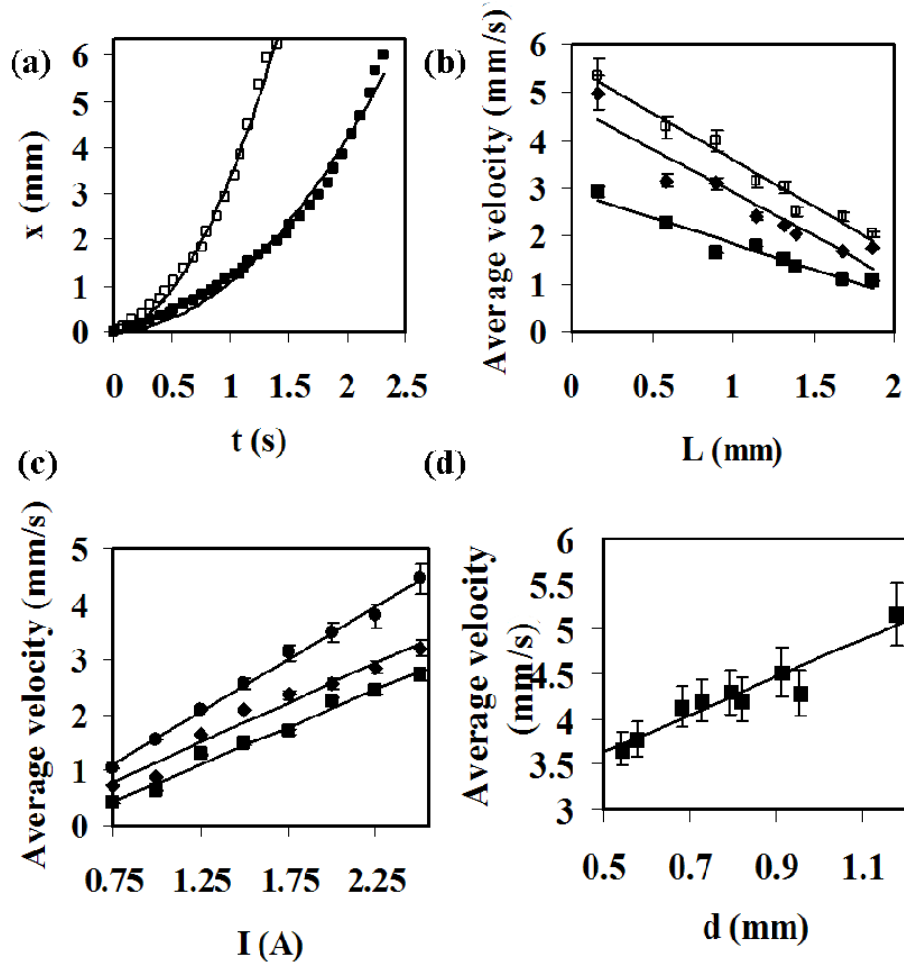


Figure 3.5: (a) The positions of an oil droplet with the diameter 0.921 ± 0.005 mm versus time when $L = 1.1 \pm 0.1$ mm. The solid lines correspond to $x = \frac{1}{2}at^2$. (Filled squares: $I = 1.5$ A, $a = 2.1$ mm/s²; the open squares: $I = 2.5$ A, $a = 6.6$ mm/s².) (b) The average velocity of an oil droplet with diameter 0.656 ± 0.005 mm versus L with different current I (Open squares: $I = 2.5$ A; filled parallelograms: $I = 2$ A; filled squares: $I = 1.5$ A). (c) The average velocity of oil droplets of different diameters (filled circles: 0.921 ± 0.005 mm; filled parallelograms: 0.656 ± 0.005 mm; filled squares: 0.457 ± 0.005 mm) versus I when $L = 1.1 \pm 0.1$ mm. (d) The average velocity of 9 oil droplets with the diameter d from 0.542 ± 0.005 mm to 1.177 ± 0.005 mm when $I = 2.5$ A and $L = 1.1 \pm 0.1$ mm. The solid lines are the best linear fits and can be used as guides for the eye.

At last we studied the effect of the droplet size on the transport velocity. The experiments were conducted using 9 oil droplets which were placed in the container simultaneously and measured one by one keeping the water surface and the position of the tips unchanged to avoid a change of L . Figure 3.5d shows the average velocity of the 9 oil droplets versus their diameters ranging from 0.542 mm to 1.177 mm when $I = 2.5\text{A}$ and $L = 1.1 \pm 0.1$ mm. The average velocities of the oil droplets increase linearly with their diameters. The narrow average velocity band, which means a narrow transport time range required to move different droplets between two fixed positions, ranging from 3.7 ± 0.2 mm/s to 5.2 ± 0.3 mm/s could facilitate the further design of the system transporting these oil droplets.

It should be noted that there are major differences in the systems described in Chapter 2 and Chapter 3. In Chapter 2, the diameters of microspheres range between $2\mu\text{m} < 2r < 36\mu\text{m}$. The microsphere moves with a constant velocity in a constant field gradient generated by a permanent magnet. The distance between the microsphere and the permanent magnet is 14.5 mm which is much larger than the displacement of the microsphere (tens of micrometers). In Chapter 3, the diameters of oil droplets range between $542\mu\text{m} < d < 1177\mu\text{m}$. The droplet accelerates in a magnetic field gradient which is not constant. The magnetic field is generated by two electromagnetic coils with tips. The sizes of the electromagnet's tips are comparable to the diameters of oil droplets. The distance between the tips and water surface is 1100 μm which is also comparable to the diameters of oil droplets. The magnetic field varies a lot in the space where the droplet is manipulated. In order to calculate the magnetic force on the droplet, we need to measure the magnetic field in three dimensions in the whole space where the droplet is manipulated. Since our aim of this work is to demonstrate a liquid-liquid microfluidic system for transporting

millimeter-sized oil droplets, we do not investigate further in the theoretical model in Chapter 3.

3.4 Conclusion

In conclusion, we have described and demonstrated a simple liquid-liquid microfluidic system for transporting free-floating oil droplets with diameters between 0.542 mm to 1.177 mm. The average velocity of these droplets increases linearly with their diameters as well as the driving electric current in the coils. Our system offers several advantageous features such as high average velocity and low energy dissipation, negligible heating and minimized influence on the transported material. Moreover, a down-scaling of the actuation system is also possible, as microcoils and microtips have previously been used to manipulate micron-sized magnetic objects [67, 68].

Chapter 4

Dynamics of magnetic bubbles in acoustic and magnetic fields

4.1 Introduction

Here we study bubbles with a magnetic moment due to a shell of self-assembled nanoparticles. We characterize their magnetic properties and demonstrate that they oscillate in an acoustic field. Some previous work has reported on very small magnetic bubbles with diameters of around $2\mu\text{m}$ - $8\mu\text{m}$ for medical use [69, 70] using either electrostatic coupling or water-oil emulsions to attach the nanoparticles to the bubble surface. Neither their magnetic properties nor their responses to an acoustic field have been measured. In contrast our new and simple recipe allows the creation of much larger and stable bubbles which we now characterize physically.

In an acoustic field, conventional free and also shelled bubbles experience two forces: a surface force compressing and expanding the gas, and additionally a radiation force caused by spatial gradients of the pressure field, the so-called Bjerknes force [71]. This Bjerknes force accelerates the bubbles into translational motion which makes it very difficult and sometimes impossible to control their oscillations and position simultaneously. An exceptional example is single bubble sonoluminescence [72] where a single bubble is trapped in the field due to the balance between buoyancy and Bjerknes force. Prior successful attempts to affect bubbles' oscillations

with magnetic fields implemented complex and costly experimental equipment [73] due to the low magnetic susceptibility of water. In contrast, the magnetic shelled bubbles reported here possess sufficient magnetization such that they can be controlled with conventional magnets, and their shell elasticity still allows for volume oscillations in moderate acoustic fields. In this chapter we first describe the recipe to create the bubbles, then we image them using an optical microscope, and the shells magnetic susceptibility is measured with a force balance model. Finally, we show the compressibility of the bubbles in moderate acoustic fields, which leads to a microstreaming flow. These observations show the great potential that magnetic bubbles have for a wide range of applications, as the bubbles can be manipulated with magnetic and acoustic fields.

4.2 A microscopic look at the magnetic bubbles

The magnetic bubbles are prepared using a simple procedure that involves self-assembly of magnetic nanoparticles: Magnetite nanoparticles were prepared in open air at room temperature as described in Chapter 2. Presumably the structure of the nanoparticles [55] is an intermediate between Fe_3O_4 and $\gamma\text{-Fe}_2\text{O}_3$. Eight milligrams of the magnetic nanoparticles were washed with 4 mL ultrapure water once, dispersed in 4 mL ultrapure water, and sonicated for ten minutes to obtain a uniform black solution. Next 500 μL of 5 mM of the surfactant sodium dodecyl sulfate (SDS, electrophoresis grade, Fisher) was added to 500 μL of the solution, and then shaken moderately for three minutes to form the magnetic bubbles.

Viewing the bubbles under a microscope reveals their metallic appearance, which is caused by a thin shell of metallic nanoparticles [55]. In Figure 4.1, the bubbles have been pipetted onto a glass slide. There, they rise to the top of the water droplet where they are imaged from above with a $5\times$ objective. The thickness of the shell has been explored with scanning electron microscopy after the bubbles have been air dried; an example of the cross section of the shell is shown in the inset of Figure 4.1. The shell thickness after drying is about 880 nm for bubbles with radii in the range of 50 to 175 μm . The scanning electron microscopy images reveal that the distribution of grains of magnetic material is not very uniform.

Interestingly, the bubbles are very stable in gas-saturated water: a sample of magnetic shelled bubbles remained intact for more than six months in a light tight lab drawer. However, when bubbles are pipetted from gas-saturated water into degassed water, they lose buoyancy and sink to the bottom. As an example, we measured a dissolution time of 700 s for a magnetic bubble with an initial radius of 148 μm in water at 35% of saturation concentration of O_2 . Comparing this time with the solution of the diffusion equation (see, for example, [74]) for a free bubble we find an increase of 2.3 times in the dissolution time which can be explained by the hindrance of the diffusion by the porous shell of the magnetic bubbles. This observation is also supported by the fact that bubbles heated in gas saturated water expand. Thus the shell of the magnetic bubble is gas permeable. The longevity of the bubbles in saturated water indicates that the arrangement of the nanoparticles in the shell is stable. In contrast, free bubbles eventually dissolve and disappear due to the Laplace pressure.

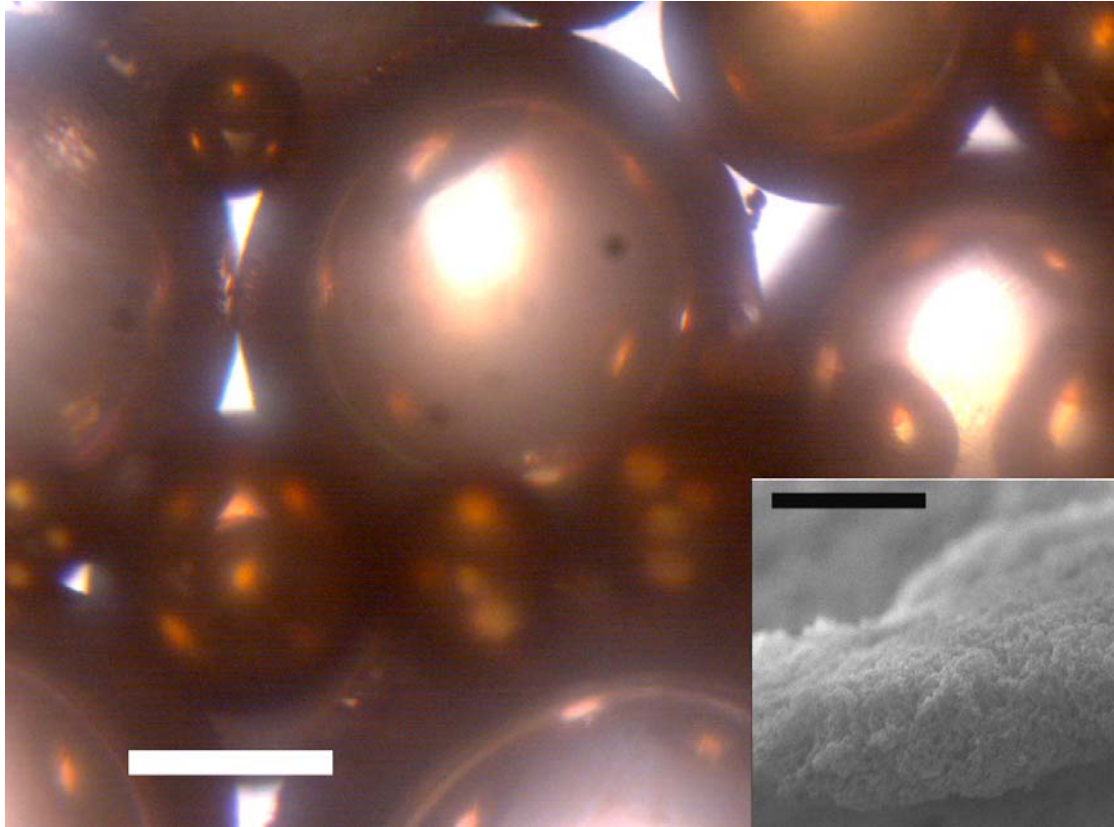


Figure 4.1: Microscopic view of magnetic bubbles: The Christmas tree ball like appearance of the magnetic bubbles is due to a thin layer of metallic nanoparticles (length of the scale bar is 300 μm). The inset shows a cross-section of the shell taken with a scanning electron microscope (length of the scale bar is 1 μm).

4.3 Magnetic susceptibility of magnetic bubbles

To measure the magnetic properties of the bubbles we used the experimental setup shown in Figure 4.2a. We let a bubble rise to the air-water interface in a transparent container; then a permanent Nd magnet is brought from below towards the container in small increments until the magnetic force overcomes buoyancy (Figure 4.2a) and

the bubble sinks to the bottom. To obtain an expression for the magnetic force [18] acting on the bubble we neglect all field gradients except the one along the y axis. Then the magnetic force in the y direction is $F_{mag} = \chi_b \mu_0^{-1} B dB/dy$, where B is the magnitude of the magnetic field, μ_0 is the permeability of vacuum, and χ_b is the magnetic susceptibility of the bubble (in units of volume). The bubble's trajectory is recorded with a digital camera (model EO1312M, Edmund Optics, NJ, USA) and modeled with Newton's 2nd law, by balancing the magnetic, buoyancy, drag, and added-mass force [75]:

$$-\frac{1}{2} \frac{d^2 y}{dt^2} V_B \rho - \frac{1}{2} \rho \pi^2 C_d \frac{dy}{dt} \left| \frac{dy}{dt} \right| + \rho V_B g - \frac{\chi_b}{\mu_0} B \frac{dB}{dy} = 0 \quad (4.1)$$

The first term represents the added-mass force due to the fluid displaced by the bubble, and the second term is the drag force, followed by buoyancy, and the magnetic force. The volume and radius of the bubble are V_B and r , respectively. Further constants are the density of the water $\rho = 10^3 \text{ kg/m}^3$ and the acceleration of gravity g . The Reynolds number is defined as $\text{Re} = 2 \left| \frac{dy}{dt} \right| r / \nu$, where $\nu = 10^{-6} \text{ m}^2/\text{s}$ is the kinematic viscosity of water. For the experiments presented here the Reynolds number ranges between 0 and 10. Therefore, a correction to the standard Stokes drag law is applied [76]; thus, the drag coefficient is $C_d = \frac{24}{\text{Re}} (1 + 0.15 \text{Re}^{0.687})$. The magnitude of the magnetic field of the Nd magnet as a function of vertical position is fitted to an exponential function $|B_y| = 0.26 \exp\left(-192.9 \frac{1}{m} y\right) \text{ T}$, where $y = 0$ corresponds to the surface of the magnet (0.26 T at the magnet's surface). As an interesting side note, the magnetic field strength to accelerate the bubble from the

surface is higher than the one needed to keep the bubble neutrally buoyant. Probably it is the surface tension which causes some activation energy in the separation of the shelled bubble from the free surface.

Figure 4.2b shows the trajectory of a bubble with a radius of $100 \pm 10 \text{ } \mu\text{m}$. The continuous line represents the fit to the model using χ_b as the only free parameter. We find very good agreement between the measurement and the model over the whole observation time. The importance of the individual forces for this particular trajectory is shown in Figure 4.2c as a function of time. As expected the added-mass force contributes only at the very late stage, when the bubble is close to the magnet and experiences largest acceleration. The strong dependence of the modeled trajectory on χ_b gives us confidence to determine the parameter through the fitting procedure. This has been done for different bubble sizes, and the result is reported in Figure 4.2d. The bubble's susceptibility is proportional to the square of the radius $\chi_b = (9 \pm 3 \times 10^{-6} \text{ m})r^2$. This agrees with the observation that the self-assembled magnetic nanoparticles form a thin shell around the bubble. It implies that the shell thickness is approximately constant for the range of bubble sizes studied. Let us now compare the measured susceptibility with the one expected from a spherical shell of magnetic material. The dimensionless susceptibility $\chi_m = 22.16$ of the Fe_3O_4 nanoparticles used in the recipe can be calculated from the magnetic dipole moment measured from the hysteresis curves of a sample of nanoparticles (averaged diameter $d = 29 \text{ nm}$) [77]. The susceptibility of a spherical shell is $\chi_b = V_{shell} f(\chi_m)$, where V_{shell} is its volume and $f(\chi_m)$ is a function of the dimensionless susceptibility χ_m given, for example, in Ref. [61]. Assuming a constant shell thickness of 880 nm we obtain $\chi_b = (0.8 - 11.7) \times 10^{-14} \text{ m}^3$ for bubbles with radii from $r = 30 \text{ } \mu\text{m}$ to

$r = 100 \mu\text{m}$. These numerical values agree nicely with the susceptibility obtained from the force balance method $\chi_b = (0.8 \pm 0.3 - 9 \pm 3) \times 10^{-14} \text{ m}^3$; see Figure 4.2d considering the uncertainty in the shell thickness.

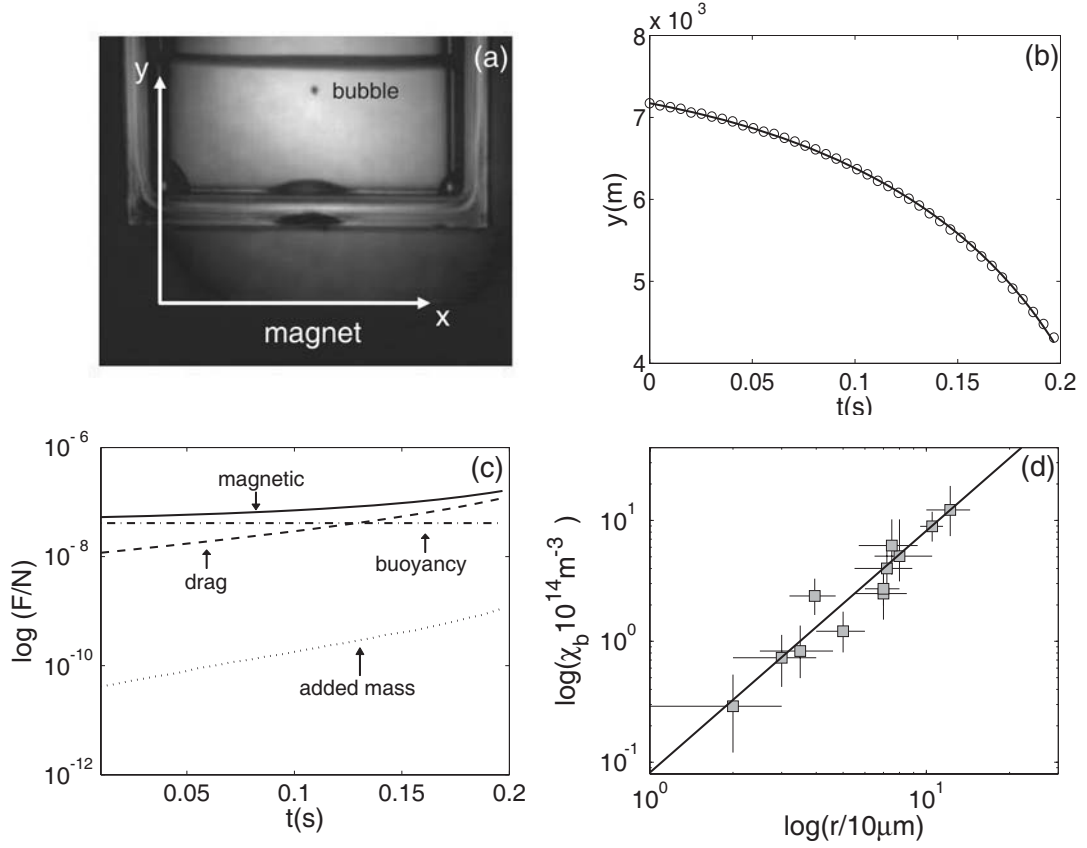


Figure 4.2: (a) Experimental setup for measuring the bubble trajectory. y axis is in the opposite direction of gravity. (b) Bubble trajectory for a $r = 100 \mu\text{m}$ bubble (circles) and fit to model (solid line). (c) Forces acting on the bubble as it sinks to the bottom of the container: magnetic (solid line), buoyancy (dashed-dot), drag (dashed) and added-mass (dotted). (d) Extracted magnetic susceptibility χ_b from a force balance model fitted to the measured trajectories (see text) and plotted as a function of radius on a log-log scale. The error bars account for the uncertainty in bubble radius, its trajectory, and the magnetic field.

4.4 The oscillation of magnetic bubbles

To study the compressibility of the magnetic shell, the bubbles are exposed to an alternating pressure field. A single bubble is placed in an acoustic container as shown in Figure 4.3a. At the closed end of the cuvette a piezo transducer (made of lead zirconate titanate material, a cylinder with a 10 mm diameter and a thickness of 5.5 mm) is attached, and the opposite side is sealed such that residual air pockets are

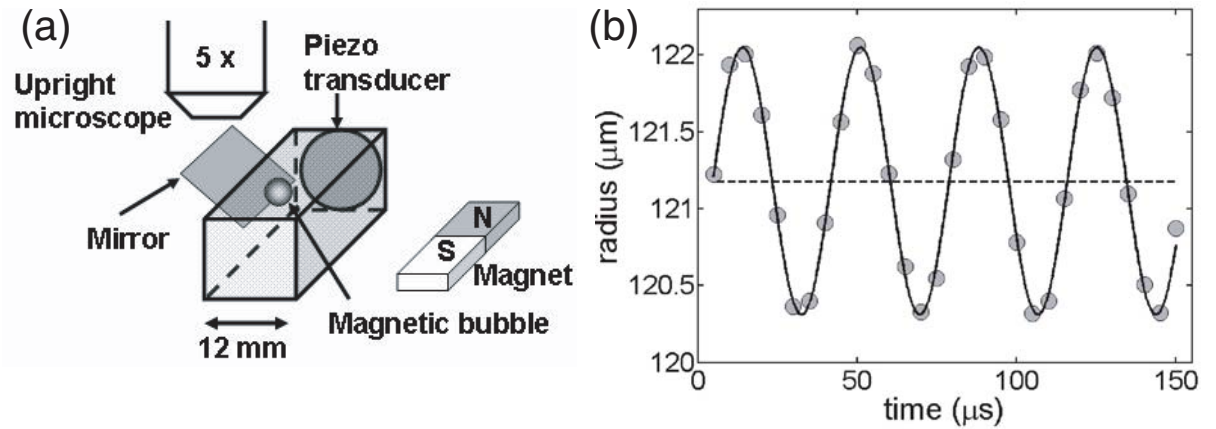


Figure 4.3: (a) Experimental setup to study bubble shell oscillations. A polystyrene cuvette with square cross-section (12mm width and 45mm length) is viewed with a microscope from the side through a mirror. The bubble located at the top is driven into volume oscillations with an acoustic field generated from a piezoelectric device glued to the back of the cuvette. (b) High-speed recordings taken at 200,000 frames/s exhibit the bubble radius as a function of time (circle) which is fitted to a sine (solid line); the driving frequency is 27 kHz.

avoided. As the cuvette is placed on its side, the bubble rises and makes contact with the top wall while retaining its mostly spherical shape. The transducer is driven with a sinusoidal voltage from a function generator connected to an amplifier and a voltage transformer. These magnetic bubbles oscillate when the frequency of the applied sound field is close to the bubble's resonance frequency. Figure 4.3b shows the shell oscillation of a bubble with a radius of $121\text{ }\mu\text{m}$ driven at 27 kHz. The bubble radius was extracted from images taken with a high-speed camera at 200,000 frames/s. The bubble contour is then fitted to a circle and its radius extracted. We find peak-to-peak variations in the bubble radius of about $1.7\text{ }\mu\text{m}$. Preliminary experiments show that although the bubble oscillations are reduced by the magnetic shell, the amplitude is of the same order of magnitude as for a free bubble. The stiffening of the shell will give a higher resonance frequency for the magnetic bubble.

It is well known that oscillating bubbles induce a microstreaming flow [78-81]. To visualize the flow, microparticles with a diameter of $3\text{ }\mu\text{m}$ (Micro particles based on polystyrene, Sigma-Aldrich) are added to the water, and as soon as the acoustic field is switched on, we observe a microstreaming flow created by the oscillating bubble. Figure 4.4a depicts the flow pattern reconstructed with particle image velocimetry using image processing software (Matlab from Mathworks). The flow velocities are estimated by cross-correlating parts of consecutive frames of the movie taken at 16.2 frames/s. This method requires that the background of the images can not include any pattern and the number of the particles must be large enough so that there are some particles within the interrogation window. The interrogation window size is 32×32 pixels and the time interval between consecutive frames is 0.06 s. In particular we find a vortex ring surrounding the upper pole of the bubble very similar to the observation of Marmottant and Hilgenfeldt [80], yet the magnetic bubble remains

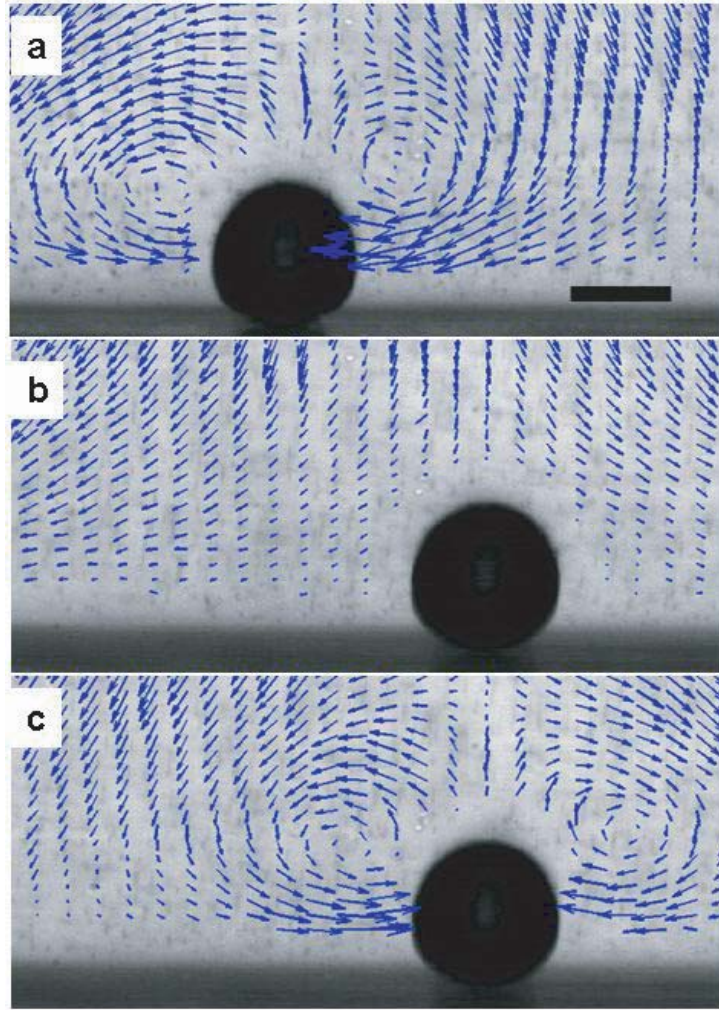


Figure 4.4: (a) Magnetic bubble-induced microstreaming. A single magnetic bubble is excited with an acoustic field driven at 41 kHz which creates a streaming flow. The flow pattern is visualized with 3 micron diameter polystyrene particles added to the water. The flow velocities are estimated by cross-correlating parts of consecutive frames (particle image velocimetry) of the movie taken at 16.2 frames/s. The interrogation window size is 32×32 pixels and the time interval between consecutive frames is 0.06 s. At resonance a vortex ring is created at the bubble's upper pole. (b) The sound field is switched off and the bubble is repositioned to the right using a permanent magnet. A residual stagnation type flow pattern remains. (c) The sound field (same amplitude and frequency) is switched on giving way to a very similar flow pattern translated to the right. The length of the scale bar is 100 μm .

spherical due to the stiff shell. When the sound field is turned off, the induced recirculating flow stops instantaneously. Then the bubble is repositioned with an external magnet (Figure 4.4b). Flow visualization exhibits a background flow which resembles a stagnation point flow. After switching on the sound field (Figure 4.4c), the bubble induced flow pattern appears again. This demonstrates that the bubble's acoustic property has not been altered. The shell is stable despite the volume oscillations and magnetic manipulation.

4.5 Conclusion

In summary we report on the physical properties of magnetic shelled bubbles prepared with a simple recipe. The bubbles cover a broad range of sizes with radii ranging from 20 μm to 175 μm ; they are exceptionally stable in gas-saturated waters for many months. Their motion in a magnetic field has been successfully modeled with a force balance. Magnetic bubbles in contrast to magnetic emulsions [82] and colloidosomes [15] offer the advantage of being able to perform volume oscillations which, for example, can drive a microstreaming flow or create locally shear stresses. We expect that magnetic bubbles may offer novel solutions for microfluidics using two independent force fields, for example, exploiting stable bubbles as remotely controlled mixers and pumps, or for the stimulation of cells with spatially and temporally controlled hydrodynamic forces.

Chapter 5

Translation of an oscillating and rising magnetic bubble

5.1 Introduction

What is the impact of a magnetic bubble's volume oscillation on its rise velocity? A bubble released in the liquid will rise, accelerating to a point where its buoyancy force is balanced by the drag force, and obtain a constant velocity. The study of rising bubbles is driven by its importance in numerous industrial processes, such as flotation tanks and stirred gas-liquid hydrogenation reactors, etc [83-90]. A large amount of work has been done in various gas-liquid systems in this subject. The experiments by de Vries et al. [90] with 2-4 mm diameter bubbles interacting with a hot-film anemometer probe in clean water show the impact of a bubble's shape oscillation on its mean velocity. To clarify how bubble volume oscillations affect the rise velocity, we make use of the magnetic bubbles and study their rise velocity once without and once with volume oscillations.

5.2 Experimental methods

The procedure used to prepare magnetic bubbles is described in Chapter 4 to which the reader is referred. A single magnetic bubble is placed in a transparent acoustic container with dimensions of 12 mm× 12 mm× 45 mm as shown in Figure 5.1. At one side of the cuvette a piezo transducer (made of lead zirconate titanate material, a cylinder with a 10 mm diameter and a thickness of 5.5 mm) is attached. The transducer is driven with a sinusoidal voltage from a function generator connected to an amplifier and a voltage transformer (high frequency transformer with a winding ratio of 1:16, Amplino B.V., The Netherlands). An electromagnet is mounted on a translation stage so that it can be moved in three dimensions in small increments. The magnetic bubble is attracted to the bottom of the cuvette by the magnetic field

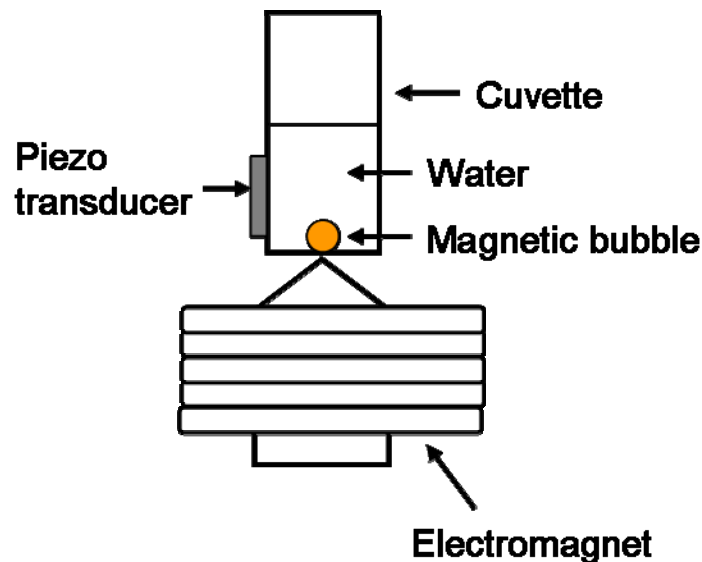


Figure 5.1: Schematics of experimental setup to measure radius and trajectory of a single magnetic bubble.

generated by the electromagnet with the current on. Then this bubble is released by switching the current off. A high speed camera (Photron SA1.1 with 10,000 frames per second) is triggered simultaneously, and the transducer is triggered 300 ms later. In this way, the bubble rises without oscillation for 300 ms; subsequently it oscillates while it rises.

The oscillation frequency of the bubble is found by sweeping from 5 kHz to 55 kHz for 100 ms when the bubble is held at the bottom. The bubble images are recorded by the high speed camera (now recording at a higher frame rate of 100,000 frames per second). When the bubble is held at the bottom, a small deformation is observed shown in Figure 5.2a. The horizontal major axis $2b_1$ and the vertical minor axis $2b_2$ of the bubble are obtained by detecting the bubble contour on each frame. The radius of the bubble is calculated assuming axisymmetry to $r = (b_1^2 b_2)^{1/3}$. The accuracy of the measurement of the radius is typically $\pm 3 \mu\text{m}$ considering the fitting error to the bubble contour, the length of each pixel and the variation of background in the image as the main error sources. Thus a small change of less than $1 \mu\text{m}$ can not be measured accurately. However, the relative change of the radius with the frequency is still a good indicator of oscillation, for example, shown in Figure 5.2b, the bubble oscillates at 50.7 kHz. This oscillation is also observed from the high speed video by bare eyes. The accuracy of the measurement of the position of the bubble center is typically $\pm 0.4 \mu\text{m}$. This high accuracy was checked by comparing the trajectory of the bubble (before the sound field was switched on) to a straight line. The position of the bubble was always less than $0.4 \mu\text{m}$ distant from the straight line. The mean rise velocity of the bubble is calculated by fitting a line to the bubble's position in 111 successive frames and measuring its slope.

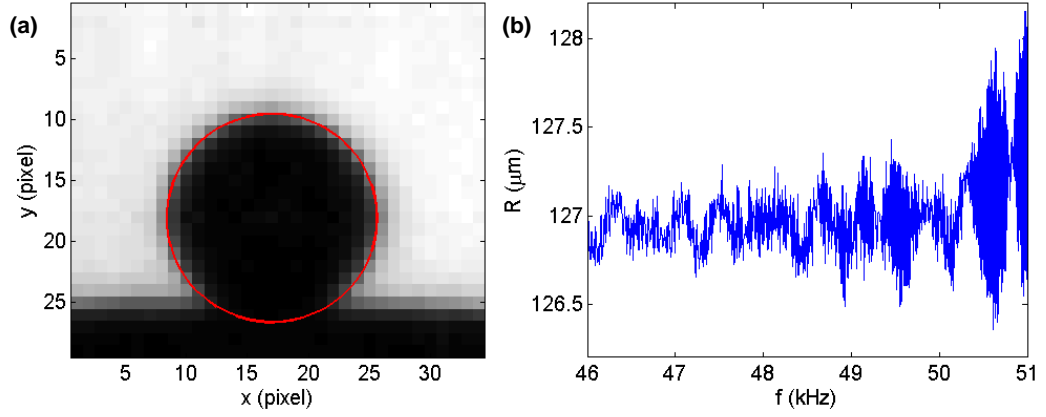


Figure 5.2: (a) A high speed image of the magnetic bubble held at the bottom of the cuvette. The red curve is the best fit of an ellipse curve to the bubble contour. The half major axis of the bubble is $b_1 = 127 \text{ } \mu\text{m}$ and the half minor axis is $b_2 = 126 \text{ } \mu\text{m}$. (b) Radial response of the magnetic bubble in the frequency ranging from 46 kHz to 51 kHz.

5.3 Results and discussion

The measured mean rise velocity before and after the volume oscillation of the magnetic bubble with radius $r = 127 \pm 3 \text{ } \mu\text{m}$ is given in solid curve in Figure 5.3. When the bubble starts to oscillate at $t = 0.3 \text{ s}$, the mean rise velocity jumps to a higher level. Here 900 images in 90 ms (time interval $1 \times 10^{-4} \text{ s}$) are used to obtain the bubble trajectory and the fluctuation of the mean rise velocity is due to the accuracy of $\pm 0.4 \text{ } \mu\text{m}$ for the position of the bubble center. The dashed curve in Figure 5.3 is the numerically calculated mean rise velocity using a force balance model.

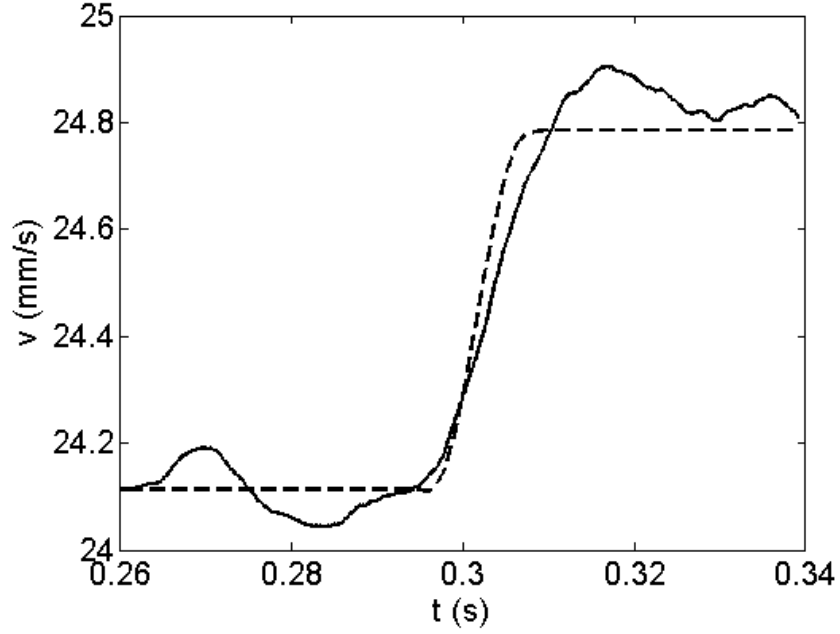


Figure 5.3: The experimental (solid) and numerically calculated (dashed) mean rise velocity v of a rising magnetic bubble with radius $r = 127 \pm 3 \mu\text{m}$. The acoustic field is turned on at $t = 0.3 \text{ s}$.

The sum of the forces acting on the bubble results in a change of momentum of the bubble,

$$\sum F = F_b + F_a + F_d + F_g + F_m = \frac{d}{dt}(mv) \approx 0, \quad (5.1)$$

where m is the mass of the magnetic bubble and v is the velocity relative to the fluid. The forces acting on the bubble are the buoyancy force F_b , the added-mass force F_a , the quasi-steady Stokes drag force F_d , the weight of the magnetic bubble F_g , and the magnetic force F_m . We assume there is no history force and the mass of the magnetic

bubble can be neglected so that the weight of the magnetic bubble F_g is equal to zero.

An extensive discussion of all forces can be found in reference [91].

The buoyancy force is

$$F_b = \frac{4}{3} \pi r(t)^3 \rho g, \quad (5.2)$$

where $r(t)$ is the radius of the bubble which changes with time when the bubble performs volume oscillation, ρ is the density of the water and g is the gravitational acceleration.

The added-mass force [75] is

$$F_a = -\frac{2}{3} \pi \rho \left(r(t)^3 \frac{d^2 y}{dt^2} + 3 \frac{dy}{dt} r(t)^2 \frac{dr(t)}{dt} \right), \quad (5.3)$$

where y is the vertical position of the rising bubble.

When the Reynolds number $\text{Re} = 2r(t) \frac{dy}{dt} / \nu$ is finite but larger than unity, the quasi-steady Stokes drag force [92] can be written as

$$F_d = -\frac{1}{2} C_d \pi r(t)^2 \rho \left(\frac{dy}{dt} \right)^2, \quad (5.4)$$

where ν is kinematic viscosity of the water and the drag coefficient C_d is taken as

$$C_d = \frac{24}{\text{Re}} (1 + 0.15 \text{Re}^{0.687}). \quad (5.5)$$

The magnetic force [57] is

$$F_m = \frac{\chi_b}{\mu_0} B \frac{dB}{dy}, \quad (5.6)$$

where B is the magnitude of the magnetic field, μ_0 is the permeability of vacuum, and χ_b is the magnetic susceptibility of the bubble which has been investigated in Chapter 4. In the present experiments, it takes 15 ms for the current to drop to zero after the signal is sent out to turn off the current of the electromagnet. When the current is zero,

the remanence of the electromagnet is measured and F_m is estimated to the order of 3×10^{-11} N in the position where the bubble is 5 mm away from the bottom. This is negligible comparing with other forces which are typically in the order of 10^{-7} N.

With equations (5.1) to (5.6) at hand, the analysis of the experimental results can be carried out. We first look at the area where the magnetic bubble is at least 5 mm away from the bottom before the magnetic bubble starts to oscillate, shown in Figure 5.4.

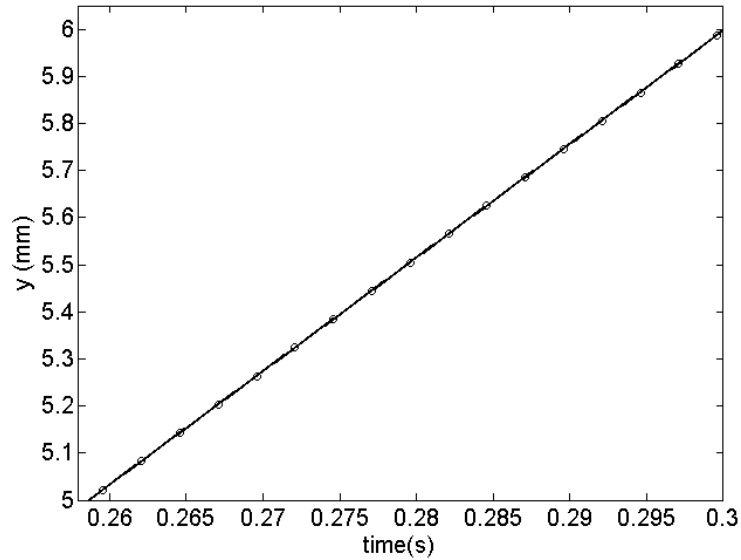


Figure 5.4: Bubble trajectory for a $r = 127 \pm 3 \mu\text{m}$ bubble (circles) before it starts to oscillate at $t = 0.3$ s, and fit to model (solid line). 454 data points are used to obtain the trajectory, but here we only draw 17 points in order to make the figure clear. The accuracy of the position measurements of the bubble center is $0.4 \mu\text{m}$. This high accuracy was checked by comparing the trajectory of the bubble (before the sound field was switched on) to a straight line. The position of the bubble was always less than $0.4 \mu\text{m}$ distant from the straight line.

Note that in this figure, $t = 0$ is the time at which the bubble is released and $y = 0$ is the position of the bubble center when $t = 0$. In this area, the radius of the bubble is constant, so that equation (5.1) can be simplified to

$$\frac{4}{3}\pi r^3 \rho g - \frac{2}{3}\pi \rho \left(r^3 \frac{d^2 y}{dt^2} \right) - \frac{1}{2} C_d \pi r^2 \rho \left(\frac{dy}{dt} \right)^2 = 0. \quad (5.7)$$

The solid line in Figure 5.4 represents the fit to equation (5.7) using r as the only free parameter. We find very good agreement between the measurement and the model with fitting value $r = 130.3 \text{ } \mu\text{m}$ which agrees with the radius measurement $127 \pm 3 \text{ } \mu\text{m}$.

Then we analyze the bubble trajectory after the acoustic field is switched on at $t = 0.3 \text{ s}$, shown in Figure 5.5. The solid line is the fit to the force balance model

$$\frac{4}{3}\pi r(t)^3 \rho g - \frac{2}{3}\pi \rho \left(r(t)^3 \frac{d^2 y}{dt^2} + 3 \frac{dy}{dt} r(t)^2 \frac{dr(t)}{dt} \right) - \frac{1}{2} C_d \pi r(t)^2 \rho \left(\frac{dy}{dt} \right)^2 = 0 \quad (5.8)$$

with the radial response to the acoustic field [93]

$$r(t) = r_c + r_a \sin(2\pi f t + \varphi), \quad (5.9)$$

where $r_c = 130.3 \text{ } \mu\text{m}$ is the parameter obtained from Figure 5.4, the resonance frequency of this magnetic bubble is $f = 50.7 \text{ kHz}$, the oscillation amplitude c and phase constant φ are two free parameters. It can be seen that the fit shows excellent agreement with the measured trajectory in Figure 5.5 with $r_a = 0.27 \text{ } \mu\text{m}$ and $\varphi = 0.1$.

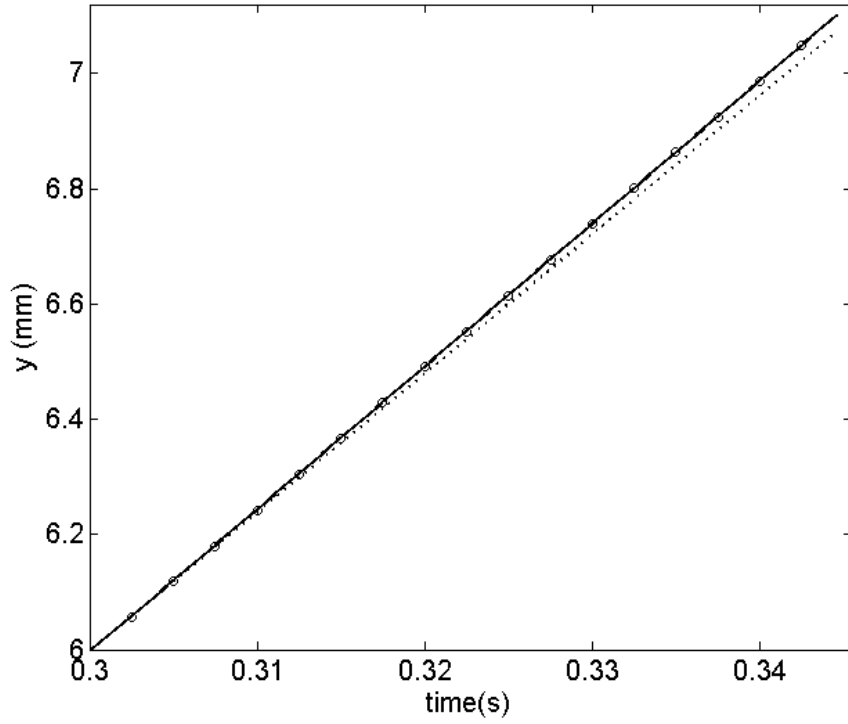


Figure 5.5: Bubble trajectory for a $r = 127 \pm 3 \mu\text{m}$ bubble (circles) when it is oscillating, and fit to model with oscillated radius (solid line) and with constant radius (dotted line). 446 data points are used to obtain the trajectory, but here we only draw 17 points in order to make the figure clear. The accuracy of the position measurements of the bubble center is $0.4 \mu\text{m}$.

We now want to study which force in equation (5.8) is responsible for the increase of the mean rise velocity. Therefore we turn off various forces in equation (5.8) and repeat the numerical calculation. The result is shown in Figure 5.6. Only if the added-mass force is included in the force balance mode, the mean rise velocity is very close to the value from the full model. So we have demonstrated that the increase of the mean rise velocity is due to the oscillating added-mass force, and not to the oscillating buoyancy force or the drag force.

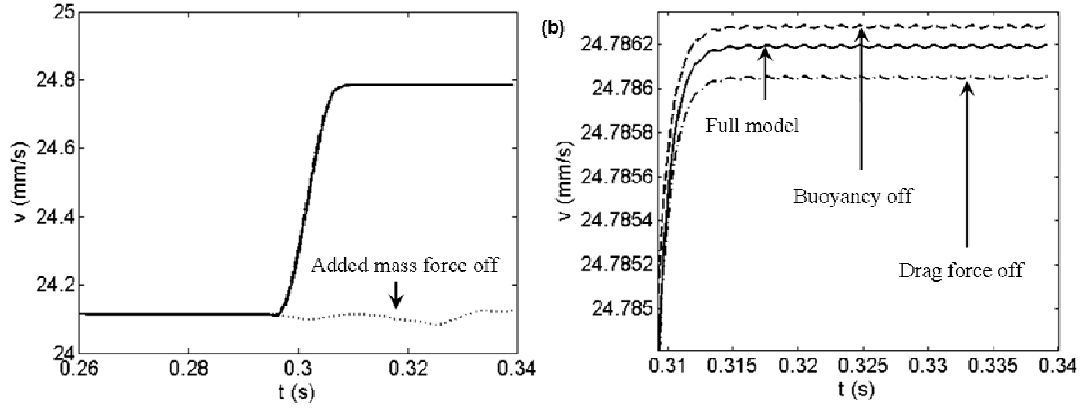


Figure 5.6: (a) The numerically calculated mean rise velocities of the magnetic bubble. The solid line corresponds to the full numerical model of equation (5.8). For the dashed line only F_a and F_d which depend on the varying radius have been employed. For the dashed-dot curve only F_b and F_a which depend on the varying radius have been employed. For the dotted curve only F_b and F_d which depend on the varying radius have been employed. (b) The zoomed in part of Figure a from time 0.31s to 0.34s.

5.4 Conclusion

In conclusion, we have performed experiments with a single $127 \mu\text{m}$ radius magnetic bubble in an acoustic field. The experiments clearly show that an oscillating magnetic bubble has a higher mean rise velocity than the same non-oscillating bubble. It is shown through a simple force balance model that the added-mass force causes the increase in the mean rise velocity for this particular set of experimental parameters.

Chapter 6

Conclusions and Future Work

6.1 Conclusions

In this thesis we have presented the results of experiments performed to investigate the physical properties of magnetic oil droplets and magnetic bubbles by self-assembly of magnetic particles at the oil-water or air-water interface. The various observations lead to the following conclusions:

- We fabricated magnetic microspheres by self-assembly of magnetic nanoparticles onto the interface of emulsion droplets and measured the magnetophoretic velocities of this kind of magnetic microspheres in a defined magnetic field. We found that larger microspheres usually have larger velocities. However, it is also clear that microspheres of the same size can have velocities that differ by more than a factor of 4. Susceptibilities of 2-35 μm magnetic microspheres have been calculated to characterize their magnetic properties. We found that χ_{sphere} is proportional to the surface area of the microsphere roughly.
- We have described and demonstrated a simple liquid-liquid microfluidic system for transporting free-floating oil droplets with diameters between 0.542 mm to 1.177 mm. The average velocity of these droplets increases linearly with their diameters as well as the driving electric current in the coils. Our

system offers several advantageous features such as high average velocity and low energy dissipation, negligible heating and minimized influence on the transported material.

- We have fabricated bubbles with a sufficient magnetization such that they can be controlled with conventional magnets. The magnetic susceptibility of the bubbles is found to be proportional to their surface area, $\chi = (9 \pm 3 \times 10^{-6} m)r^2$, where r is the radius. The elasticity of their magnetic shells allows for volume oscillations in moderate acoustic fields and induces a microstreaming flow with a toroidal vortex at the upper pole of the bubble.
- We have conducted experiments clearly showing that the volume oscillating magnetic bubble after the acoustic field is switched on has 3% higher mean rise velocity than the non-oscillating bubble before the acoustic field is switched on. With the help of a force balance model we find that the increase of mean rise velocity is due to an added-mass effect.

6.2 Future work

For the transport of free-floating droplets using electromagnetic coils, the principle presented here could be extended to an array of electromagnetic coils in order to transport floating droplets in two dimensions in a controllable way. The driving current of each electromagnetic coil can be controlled to be on or off in a specific time interval by a programmable logic device. Furthermore, such a device would in principle allow one to transport multiple oil droplets containing different samples, which could be mixed if they reach the same destination and coalesce.

For the magnetic bubbles, the shells of the magnetic bubbles make them stable to disproportionation, and allow for volume oscillations in moderate acoustic fields. Further experiments with AFM might help us to get a better understanding of the elastic properties of the magnetic shells composed of nanoparticles. AFM approach has been used to study the elastic properties of the polyelectrolyte microcapsule shells [94]. The Young's modulus of the capsule shell is obtained by fitting load-deformation curves to the predictions of the model.

Magnetic bubbles may offer novel solutions for micro-fluidics, e.g. exploiting stable bubbles as remotely controlled mixers and pumps, or for the stimulation of cells with spatial and temporal controlled shear stresses.

References

1. A. D. Dinsmore, M. F. Hsu, M. G. Nikolaides, M. Marquez, A. R. Bausch, and D. A. Weitz, "Colloidosomes: Selectively permeable capsules composed of colloidal particles," *Science* **298**, 1006-1009 (2002).
2. S. Levine, B. D. Bowen, and S. J. Partridge, "Stabilization of emulsions by fine particles .1. Partitioning of particles between continuous phase and oil-water interface," *Colloids and Surfaces* **38**, 325-343 (1989).
3. S. U. Pickering, "Emulsions," *Journal of the Chemical Society* **91**, 2001-2021 (1907).
4. P. Finkle, H. D. Draper, and J. H. Hildebrand, "The theory of emulsification," *J. Am. Chem. Soc.* **45**, 2780-2788 (1923).
5. J. H. Schulman, and J. Leja, "Control of contact angles at the oil-water-solid interfaces - emulsions stabilized by solid particles (BaSO_4)," *Transactions of the Faraday Society* **50**, 598-605 (1954).
6. B. P. Binks, and S. O. Lumsdon, "Influence of particle wettability on the type and stability of surfactant-free emulsions," *Langmuir* **16**, 8622-8631 (2000).
7. B. P. Binks, and S. O. Lumsdon, "Pickering emulsions stabilized by monodisperse latex particles: Effects of particle size," *Langmuir* **17**, 4540-4547 (2001).
8. N. P. Ashby, and B. P. Binks, "Pickering emulsions stabilised by laponite clay particles," *PCCP Phys. Chem. Chem. Phys.* **2**, 5640-5646 (2000).

9. S. Abend, N. Bonnke, U. Gutschner, and G. Lagaly, "Stabilization of emulsions by heterocoagulation of clay minerals and layered double hydroxides," *Colloid Polym. Sci.* **276**, 730-737 (1998).
10. B. P. Binks, W. H. Liu, and J. A. Rodrigues, "Novel stabilization of emulsions via the heteroaggregation of nanoparticles," *Langmuir* **24**, 4443-4446 (2008).
11. N. D. Denkov, I. B. Ivanov, P. A. Kralchevsky, and D. T. Wasan, "A possible mechanism of stabilization of emulsions by solid particles," *Journal of Colloid and Interface Science* **150**, 589-593 (1992).
12. A. Tsugita, S. Takemoto, K. Mori, T. Yoneya, and Y. Otani, "Studies on o/w emulsions stabilized with insoluble montmorillonite-organic complexes," *Journal of Colloid and Interface Science* **95**, 551-560 (1983).
13. D. E. Tambe, and M. M. Sharma, "Factors controlling the stability of colloid-stabilized emulsions .1. An experimental investigation," *Journal of Colloid and Interface Science* **157**, 244-253 (1993).
14. B. Samanta, D. Patra, C. Subramani, Y. Ofir, G. Yesilbag, A. Sanyal, and V. M. Rotello, "Stable magnetic colloidosomes via click-mediated crosslinking of nanoparticles at water-oil interfaces," *Small* **5**, 685-688 (2009).
15. H. W. Duan, D. Y. Wang, N. S. Sobal, M. Giersig, D. G. Kurth, and H. Mohwald, "Magnetic colloidosomes derived from nanoparticle interfacial self-assembly," *Nano Lett.* **5**, 949-952 (2005).
16. Q. A. Pankhurst, J. Connolly, S. K. Jones, and J. Dobson, "Applications of magnetic nanoparticles in biomedicine," *Journal of Physics D-Applied Physics* **36**, R167-R181 (2003).
17. D. L. Graham, H. A. Ferreira, and P. P. Freitas, "Magnetoresistive-based biosensors and biochips," *Trends Biotechnol.* **22**, 455-462 (2004).

18. M. A. M. Gijs, "Magnetic bead handling on-chip: New opportunities for analytical applications," *Microfluid. Nanofluid.* **1**, 22-40 (2004).
19. S. J. Gill, C. P. Malone, and M. Downing, "Magnetic susceptibility measurements of single small particles," *Rev. Sci. Instrum.* **31**, 1299-1303 (1960).
20. U. O. Hafeli, M. A. Lobedann, J. Steingroewer, L. R. Moore, and J. Riffle, "Optical method for measurement of magnetophoretic mobility of individual magnetic microspheres in defined magnetic field," in *5th International Conference on Scientific and Clinical Applications of Magnetic Carriers*(Elsevier Science Bv, Lyon, FRANCE, 2004), pp. 224-239.
21. K. van Ommering, J. H. Nieuwenhuis, L. J. van Ijzendoorn, B. Koopmans, and M. W. J. Prins, "Confined brownian motion of individual magnetic nanoparticles on a chip: Characterization of magnetic susceptibility," *Appl. Phys. Lett.* **89**, 3 (2006).
22. M. Suwa, and H. Watarai, "Magnetophoretic velocimetry of manganese(ii) in a single emulsion droplet at the femtomole level," *Analytical Chemistry* **73**, 5214-5219 (2001).
23. K. Jensen, and A. Lee, "The science & applications of droplets in microfluidic devices - foreword," *Lab Chip* **4**, 31N-32N (2004).
24. K. D. Barton, and R. S. Subramanian, "The migration of liquid-drops in a vertical temperature-gradient," *Journal of Colloid and Interface Science* **133**, 211-222 (1989).
25. T. S. Sammarco, and M. A. Burns, "Thermocapillary pumping of discrete drops in microfabricated analysis devices," *Aiche J.* **45**, 350-366 (1999).

26. M. K. Chaudhury, and G. M. Whitesides, "How to make water run uphill," *Science* **256**, 1539-1541 (1992).
27. K. Ichimura, S. K. Oh, and M. Nakagawa, "Light-driven motion of liquids on a photoresponsive surface," *Science* **288**, 1624-1626 (2000).
28. M. Washizu, "Electrostatic actuation of liquid droplets for microreactor applications," in *Industry-Applications-Society Annual Meeting*(Ieee-Inst Electrical Electronics Engineers Inc, New Orleans, Louisiana, 1997), pp. 732-737.
29. M. G. Pollack, R. B. Fair, and A. D. Shenderov, "Electrowetting-based actuation of liquid droplets for microfluidic applications," *Appl. Phys. Lett.* **77**, 1725-1726 (2000).
30. O. D. Velev, B. G. Prevo, and K. H. Bhatt, "On-chip manipulation of free droplets," *Nature* **426**, 515-516 (2003).
31. T. Ohashi, H. Kuyama, K. Suzuki, and S. Nakamura, "Control of aqueous droplets using magnetic and electrostatic forces," *Anal. Chim. Acta* **612**, 218-225 (2008).
32. U. Lehmann, S. Hadjidj, V. K. Parashar, C. Vandevyver, A. Rida, and M. A. M. Gijs, "Two-dimensional magnetic manipulation of microdroplets on a chip as a platform for bioanalytical applications," in *13th International Conference on Solid-State Sensors, Actuators and Microsystems*(Elsevier Science Sa, Seoul, SOUTH KOREA, 2005), pp. 457-463.
33. N. T. Nguyen, K. M. Ng, and X. Y. Huang, "Manipulation of ferrofluid droplets using planar coils," *Appl. Phys. Lett.* **89**, 3 (2006).

34. X. Hong, X. F. Gao, and L. Jiang, "Application of superhydrophobic surface with high adhesive force in no lost transport of superparamagnetic microdroplet," *J. Am. Chem. Soc.* **129**, 1478-1479 (2007).
35. S. I. Kam, and W. R. Rossen, "Anomalous capillary pressure, stress, and stability of solids-coated bubbles," *Journal of Colloid and Interface Science* **213**, 329-339 (1999).
36. Z. P. Du, M. P. Bilbao-Montoya, B. P. Binks, E. Dickinson, R. Ettelaie, and B. S. Murray, "Outstanding stability of particle-stabilized bubbles," *Langmuir* **19**, 3106-3108 (2003).
37. E. Dickinson, R. Ettelaie, T. Kostakis, and B. S. Murray, "Factors controlling the formation and stability of air bubbles stabilized by partially hydrophobic silica nanoparticles," *Langmuir* **20**, 8517-8525 (2004).
38. T. Kostakis, R. Ettelaie, and B. S. Murray, "Effect of high salt concentrations on the stabilization of bubbles by silica particles," *Langmuir* **22**, 1273-1280 (2006).
39. R. G. Alargova, D. S. Warhadpande, V. N. Paunov, and O. D. Velev, "Foam superstabilization by polymer microrods," *Langmuir* **20**, 10371-10374 (2004).
40. B. P. Binks, and T. S. Horozov, "Aqueous foams stabilized solely by silica nanoparticles," *Angew. Chem.-Int. Edit.* **44**, 3722-3725 (2005).
41. M. Abkarian, A. B. Subramaniam, S. H. Kim, R. J. Larsen, S. M. Yang, and H. A. Stone, "Dissolution arrest and stability of particle-covered bubbles," *Phys. Rev. Lett.* **99**, 4 (2007).
42. W. Ramsden, "Separation of solids in the surface-layers of solutions and 'suspensions' (observations on surface-membranes, bubbles, emulsions, and mechanical coagulation). Preliminary account.," *Proc. R. Soc. London* **72**, 156-164 (1903).

43. H. Xu, S. Melle, K. Golemanov, and G. Fuller, "Shape and buckling transitions in solid-stabilized drops," *Langmuir* **21**, 10016-10020 (2005).
44. C. D. Ohl, M. Arora, R. Dijkink, V. Janve, and D. Lohse, "Surface cleaning from laser-induced cavitation bubbles," *Appl. Phys. Lett.* **89**, 3 (2006).
45. K. S. Suslick, "Sonochemistry," *Science* **247**, 1439-1445 (1990).
46. W. B. McNamara, Y. T. Didenko, and K. S. Suslick, "Sonoluminescence temperatures during multi-bubble cavitation," *Nature* **401**, 772-775 (1999).
47. K. Wei, A. R. Jayaweera, S. Firoozan, A. Linka, D. M. Skyba, and S. Kaul, "Quantification of myocardial blood flow with ultrasound-induced destruction of microbubbles administered as a constant venous infusion," *Circulation* **97**, 473-483 (1998).
48. P. N. Burns, S. R. Wilson, and D. H. Simpson, "Pulse inversion imaging of liver blood flow - improved method for characterizing focal masses with microbubble contrast," *Invest. Radiol.* **35**, 58-71 (2000).
49. T. K. Kim, B. I. Choi, J. K. Han, H. S. Hong, S. H. Park, and S. G. Moon, "Hepatic tumors: Contrast agent-enhancement patterns with pulse-inversion harmonic us," in *85th Annual Meeting and Scientific-Assembly-of-the-Radiological-Society-of-North-America*(Radiological Soc North Amer, Chicago, Illinois, 1999), pp. 411-417.
50. F. Yang, A. Y. Gu, Z. P. Chen, N. Gu, and M. Ji, "Multiple emulsion microbubbles for ultrasound imaging," *Materials Letters* **62**, 121-124 (2008).
51. E. C. Unger, T. Porter, W. Culp, R. Labell, T. Matsunaga, and R. Zutshi, "Therapeutic applications of lipid-coated microbubbles," *Adv. Drug Deliv. Rev.* **56**, 1291-1314 (2004).

52. T. L. Li, K. Tachibana, and M. Kuroki, "Gene transfer with echo-enhanced contrast agents: Comparison between albutex, optison, and levovist in mice - initial results," *Radiology* **229**, 423-428 (2003).
53. L. E. Helseth, R. M. Muruganathan, Y. Zhang, and T. M. Fischer, "Colloidal rings in a liquid mixture," *Langmuir* **21**, 7271-7275 (2005).
54. C. Zeng, H. Bissig, and A. D. Dinsmore, "Particles on droplets: From fundamental physics to novel materials," *Solid State Communications* **139**, 547-556 (2006).
55. M. Tada, S. Hatanaka, H. Sanbonsugi, N. Matsushita, and M. Abe, "Method for synthesizing ferrite nanoparticles similar to 30 nm in diameter on neutral pH condition for biomedical applications," in *47th Annual Conference on Magnetism and Magnetic Materials*(Tampa, Florida, 2002), pp. 7566-7568.
56. J. A. Reynolds, and C. Tanford, "Binding of dodecyl sulfate to proteins at high binding ratios - possible implications for state of proteins in biological membranes," *Proceedings of the National Academy of Sciences of the United States of America* **66**, 1002-1007 (1970).
57. R. Gerber, and R. R. Birss, *High gradient magnetic separation* (Wiley, New York, 1983).
58. G. P. Hatch, and R. E. Stelter, "Magnetic design considerations for devices and particles used for biological high-gradient magnetic separation (hgms) systems," in *3rd International Conference on Scientific and Clinical Applications of Magnetic Carriers*(Rostock, Germany, 2000), pp. 262-276.
59. C. X. Liu, L. Lagae, R. Wirix-Speetjens, and G. Borghs, "On-chip separation of magnetic particles with different magnetophoretic mobilities," *Journal of Applied Physics* **101** (2007).

60. S. W. Yuan, *Foundations of fluid mechanics* (Prentice-Hall, Inc., Englewood cliffs, Nj, 1967).
61. J. D. Jackson, *Classical electrodynamics* (John Wiley & Sons, New York, 1998).
62. P. Ganatos, R. Pfeffer, and S. Weinbaum, "A strong interaction theory for the creeping motion of a sphere between plane parallel boundaries .2. Parallel motion," *Journal of Fluid Mechanics* **99**, 755-783 (1980).
63. W. B. Song, Z. W. Ding, C. Son, and B. Ziaie, "Aqueous microdrop manipulation and mixing using ferrofluid dynamics," *Appl. Phys. Lett.* **90** (2007).
64. Y. Sun, Y. C. Kwok, and N. T. Nguyen, "A circular ferrofluid driven microchip for rapid polymerase chain reaction," *Lab Chip* **7**, 1012-1017 (2007).
65. A. Beyzavi, and N. T. Nguyen, "One-dimensional actuation of a ferrofluid droplet by planar microcoils," *Journal of Physics D-Applied Physics* **42** (2009).
66. N. T. Nguyen, A. Beyzavi, K. M. Ng, and X. Y. Huang, "Kinematics and deformation of ferrofluid droplets under magnetic actuation," *Microfluid. Nanofluid.* **3**, 571-579 (2007).
67. M. Barbic, J. J. Mock, A. P. Gray, and S. Schultz, "Scanning probe electromagnetic tweezers," *Appl. Phys. Lett.* **79**, 1897-1899 (2001).
68. M. Barbic, J. J. Mock, A. P. Gray, and S. Schultz, "Electromagnetic micromotor for microfluidics applications," *Appl. Phys. Lett.* **79**, 1399-1401 (2001).
69. K. Soetanto, and H. Watarai, "Development of magnetic microbubbles for drug delivery system (dds)," in *20th Memorial Symposium on Ultrasonic Electronics (USE 99)*(Japan J Applied Physics, Japan, 1999), pp. 3230-3232.
70. F. Yang, Y. X. Li, Z. P. Chen, Y. Zhang, J. R. Wu, and N. Gu, "Superparamagnetic iron oxide nanoparticle-embedded encapsulated

- microbubbles as dual contrast agents of magnetic resonance and ultrasound imaging," *Biomaterials* **30**, 3882-3890 (2009).
71. T. G. Leighton, *The acoustic bubble* (Academic Press, London, 1997).
 72. M. P. Brenner, S. Hilgenfeldt, and D. Lohse, "Single-bubble sonoluminescence," *Reviews of Modern Physics* **74**, 425-484 (2002).
 73. J. B. Young, T. Schmiedel, and W. Kang, "Sonoluminescence in high magnetic fields," *Phys. Rev. Lett.* **77**, 4816-4819 (1996).
 74. O. A. Sapozhnikov, V. A. Khokhlova, M. R. Bailey, J. C. Williams, J. A. McAteer, R. O. Cleveland, and C. A. Crum, "Effect of overpressure and pulse repetition frequency on cavitation in shock wave lithotripsy," *Journal of the Acoustical Society of America* **112**, 1183-1195 (2002).
 75. C. D. Ohl, A. Tijink, and A. Prosperetti, "The added mass of an expanding bubble," *Journal of Fluid Mechanics* **482**, 271-290 (2003).
 76. R. Clift, J. R. Grace, and M. E. Weber, *Bubbles, drops, and particles* (Academic Press, New York, 1978).
 77. X. Zhao, and L. E. Helseth, "Magnetophoresis of microspheres covered by magnetic nanoparticles," *Journal of Applied Physics* **102** (2007).
 78. J. Lighthill, "Acoustic streaming," *Journal of Sound and Vibration* **61**, 391-418 (1978).
 79. M. S. Longuet-Higgins, "Viscous streaming from an oscillating spherical bubble," *Proceedings of the Royal Society of London Series a-Mathematical Physical and Engineering Sciences* **454**, 725-742 (1998).
 80. P. Marmottant, and S. Hilgenfeldt, "Controlled vesicle deformation and lysis by single oscillating bubbles," *Nature* **423**, 153-156 (2003).

81. P. Marmottant, J. P. Raven, H. Gardeniers, J. G. Bomer, and S. Hilgenfeldt, "Microfluidics with ultrasound-driven bubbles," *Journal of Fluid Mechanics* **568**, 109-118 (2006).
82. S. Melle, M. Lask, and G. G. Fuller, "Pickering emulsions with controllable stability," *Langmuir* **21**, 2158-2162 (2005).
83. A. A. Kulkarni, and J. B. Joshi, "Bubble formation and bubble rise velocity in gas-liquid systems: A review," *Ind. Eng. Chem. Res.* **44**, 5873-5931 (2005).
84. S. T. Thoroddsen, T. G. Etoh, and K. Takehara, "High-speed imaging of drops and bubbles," *Annual Review of Fluid Mechanics* **40**, 257-285 (2008).
85. L. Parkinson, R. Sedev, D. Fornasiero, and J. Ralston, "The terminal rise velocity of 10-100 μm diameter bubbles in water," *Journal of Colloid and Interface Science* **322**, 168-172 (2008).
86. C. Veldhuis, A. Biesheuvel, and L. Van Wijngaarden, "Shape oscillations on bubbles rising in clean and in tap water," *Physics of Fluids* **20** (2008).
87. M. M. Wu, and M. Gharib, "Experimental studies on the shape and path of small air bubbles rising in clean water," *Physics of Fluids* **14**, L49-L52 (2002).
88. S. Bando, and F. Takemura, "Rise speed of supercritical carbon dioxide spheres in aqueous surfactant solutions," *Journal of Fluid Mechanics* **548**, 133-140 (2006).
89. W. C. Park, J. F. Klausner, and R. Mei, "Unsteady forces on spherical bubbles," *Experiments in Fluids* **19**, 167-172 (1995).
90. J. de Vries, S. Luther, and D. Lohse, "Induced bubble shape oscillations and their impact on the rise velocity," *European Physical Journal B* **29**, 503-509 (2002).
91. G. K. Batchelor, *An introduction to fluid dynamics* (Cambridge University Press, Cambridge, 1970).

92. F. Takemura, and J. Magnaudet, "The history force on a rapidly shrinking bubble rising at finite reynolds number," *Physics of Fluids* **16**, 3247-3255 (2004).
93. X. Zhao, P. A. Quinto-Su, and C. D. Ohl, "Dynamics of magnetic bubbles in acoustic and magnetic fields," *Phys. Rev. Lett.* **102** (2009).
94. V. V. Lulevich, and O. I. Vinogradova, "Effect of pH and salt on the stiffness of polyelectrolyte multilayer microcapsules," *Langmuir* **20**, 2874-2878 (2004).